

Structure of photosystem II and substrate binding at room temperature

Iris D. Young^{1*}, Mohamed Ibrahim^{2*}, Ruchira Chatterjee^{1*}, Sheraz Gul¹, Franklin D. Fuller¹, Sergey Koroidov³, Aaron S. Brewster¹, Rosalie Tran¹, Roberto Alonso-Mori⁴, Thomas Kroll^{5,6}, Tara Michels-Clark¹, Hartawan Laksmono⁵, Raymond G. Sierra^{4,5}, Claudio A. Stan⁵, Rana Hussein², Miao Zhang², Lacey Douthit¹, Markus Kubin⁷, Casper de Lichtenberg³, Long Vo Pham³, Håkan Nilsson³, Mun Hon Cheah³, Dmitriy Shevela³, Claudio Saracini¹, Mackenzie A. Bean¹, Ina Seuffert², Dimosthenis Sokaras⁶, Tsu-Chien Weng^{6†}, Ernest Pastor¹, Clemens Weninger⁵, Thomas Fransson⁵, Louise Lassalle¹, Philipp Bräuer^{8,9}, Pierre Aller⁹, Peter T. Docker⁹, Babak Andi¹⁰, Allen M. Orville⁹, James M. Glownia⁴, Silke Nelson⁴, Marcin Sikorski¹⁴, Diling Zhu⁴, Mark S. Hunter⁴, Thomas J. Lane⁴, Andy Aquila⁴, Jason E. Koglin⁴, Joseph Robinson⁴, Mengning Liang⁴, Sébastien Boutet⁴, Artem Y. Lyubimov^{11,12}, Monarin Uervirojnangkoorn^{11,12}, Nigel W. Moriarty¹, Dorothée Liebschner¹, Pavel V. Afonine¹, David G. Waterman^{13,14}, Gwyndaf Evans⁹, Philippe Wernet⁷, Holger Dobbek², William I. Weis^{11,15,16}, Axel T. Brunger^{11,12,15,16}, Petrus H. Zwart¹, Paul D. Adams^{1,17}, Athina Zouni², Johannes Messinger^{3,18}, Uwe Bergmann⁵, Nicholas K. Sauter¹, Jan Kern^{1,4}, Vittal K. Yachandra¹ & Junko Yano¹

Light-induced oxidation of water by photosystem II (PS II) in plants, algae and cyanobacteria has generated most of the dioxygen in the atmosphere. PS II, a membrane-bound multi-subunit pigment protein complex, couples the one-electron photochemistry at the reaction centre with the four-electron redox chemistry of water oxidation at the Mn₄CaO₅ cluster in the oxygen-evolving complex (OEC). Under illumination, the OEC cycles through five intermediate S-states (S₀ to S₄)¹, in which S₁ is the dark-stable state and S₃ is the last semi-stable state before O–O bond formation and O₂ evolution^{2,3}. A detailed understanding of the O–O bond formation mechanism remains a challenge, and will require elucidation of both the structures of the OEC in the different S-states and the binding of the two substrate waters to the catalytic site^{4–6}. Here we report the use of femtosecond pulses from an X-ray free electron laser (XFEL) to obtain damage-free, room temperature structures of dark-adapted (S₁), two-flash illuminated (2F; S₃-enriched), and ammonia-bound two-flash illuminated (2F-NH₃; S₃-enriched) PS II. Although the recent 1.95 Å resolution structure of PS II at cryogenic temperature using an XFEL⁷ provided a damage-free view of the S₁ state, measurements at room temperature are required to study the structural landscape of proteins under functional conditions^{8,9}, and also for *in situ* advancement of the S-states. To investigate the water-binding site(s), ammonia, a water analogue, has been used as a marker, as it binds to the Mn₄CaO₅ cluster in the S₂ and S₃ states¹⁰. Since the ammonia-bound OEC is active, the ammonia-binding Mn site is not a substrate water site^{10–13}. This approach, together with a comparison of the native dark and 2F states, is used to discriminate between proposed O–O bond formation mechanisms.

Diffraction to 2.0 Å was observed at room temperature and structural datasets for the S₁ and 2F states of PS II (Fig. 1a, b and Extended Data Fig. 1a) under different buffer conditions were obtained at 3.0 to 2.25 Å resolution (see Methods, Extended Data Table 1 and Supplementary Tables 1–4). The packing of the PS II dimers (Fig. 1c) and unit cell

dimensions differ significantly from those reported in ref. 7 (Extended Data Fig. 1). For the illuminated data, the unit cell dimensions remained the same as for the S₁-state data, in contrast to a recent report¹⁴ (see also ref. 15). Examples of the electron densities ($2mF_o - DF_c$ and polder bulk solvent-excluding omit maps, see Methods) for several structural groups are shown in Fig. 1d–f and Extended Data Fig. 2 for the S₁ state (3.0 Å resolution) and the 2F state, with and without ammonia (at 2.8 and 2.25 Å resolution, respectively).

Compared to the cryogenic S₁ XFEL structure⁷, large-scale rotation of the monomers relative to each other by approximately 0.6° in the dimeric complex is observed in our room temperature S₁ XFEL structure. Within each monomer, the locations and orientations of transmembrane helices (TMHs) also differ, resulting in expansion of each monomer within the membrane (Fig. 2a and Extended Data Fig. 3). We also observe systematic elongation of the centre-to-centre distances between the cofactors of the electron transport chain by 0.1–0.4 Å (Fig. 2b and Extended Data Fig. 4a) and expansion of distances between adjacent chlorophyll centres involved in energy transfer in the antennae (CP43, CP47) (Fig. 2c, Extended Data Fig. 4b–d and Supplementary Table 5) by 1–3.5% (0.3–0.9 Å) compared to the cryogenic S₁ XFEL structure⁷. Changes of this magnitude are larger than the errors for the cofactors in our structure (Methods and Supplementary Table 5). Comparison of our room temperature S₁ XFEL structure with the cryogenic S₁ XFEL structure⁷ and a cryogenic S₁ synchrotron radiation structure¹⁶ that featured dimer packing similar to our room temperature XFEL structure (Extended Data Figs 3, 4 and Supplementary Information) reveals that the majority of changes in TMH positions and cofactor distances are the result of the difference in data collection temperatures. Differences in the equilibrium distances have a profound influence on the calculated electron and excitation transfer rates in PS II. For example, extension of the pheophytin (Pheo)_{D1}–QA (primary acceptor plastoquinone bound to PS II) distance by 0.2 Å leads to a reduction in the calculated electron transfer

¹Molecular Biophysics and Integrated Bioimaging Division, Lawrence Berkeley National Laboratory, Berkeley, California 94720, USA. ²Institut für Biologie, Humboldt-Universität zu Berlin, D-10099 Berlin, Germany. ³Institutionen för Kemi, Kemiskt Biologiskt Centrum, Umeå Universitet, SE 90187 Umeå, Sweden. ⁴LCLS, SLAC National Accelerator Laboratory, Menlo Park, California 94025, USA. ⁵Stanford PULSE Institute, SLAC National Accelerator Laboratory, Menlo Park, California 94025, USA. ⁶SSRL, SLAC National Accelerator Laboratory, Menlo Park, California 94025, USA. ⁷Institute for Methods and Instrumentation on Synchrotron Radiation Research, Helmholtz Zentrum, 14109 Berlin, Germany. ⁸Department of Biochemistry, University of Oxford, South Parks Road, Oxford OX1 3QU, UK. ⁹Diamond Light Source Ltd, Harwell Science and Innovation Campus, Didcot, Oxfordshire OX11 0DE, UK. ¹⁰National Synchrotron Light Source II, Brookhaven National Laboratory, Upton, New York 11793, USA. ¹¹Department of Molecular and Cellular Physiology, Stanford University, Stanford, California 94305, USA. ¹²Howard Hughes Medical Institute, Stanford University, California 94305, USA. ¹³STFC Rutherford Appleton Laboratory, Didcot, Oxfordshire OX11 0QX, UK. ¹⁴CCP4, Research Complex at Harwell, Rutherford Appleton Laboratory, Didcot, Oxfordshire OX11 0FA, UK. ¹⁵Department of Photon Science, Stanford University, Stanford, California 94305, USA. ¹⁶Department of Structural Biology, Stanford University, Stanford, California 94305, USA. ¹⁷Department of Bioengineering, University of California Berkeley, Berkeley, California 94720, USA. ¹⁸Department of Chemistry, Molecular Biomimetics, Ångström Laboratory, Uppsala University, SE 75237 Uppsala, Sweden. [†]Present address: Center for High Pressure Science & Technology Advanced Research, Pudong, Shanghai 201203, China.
*These authors contributed equally to this work.

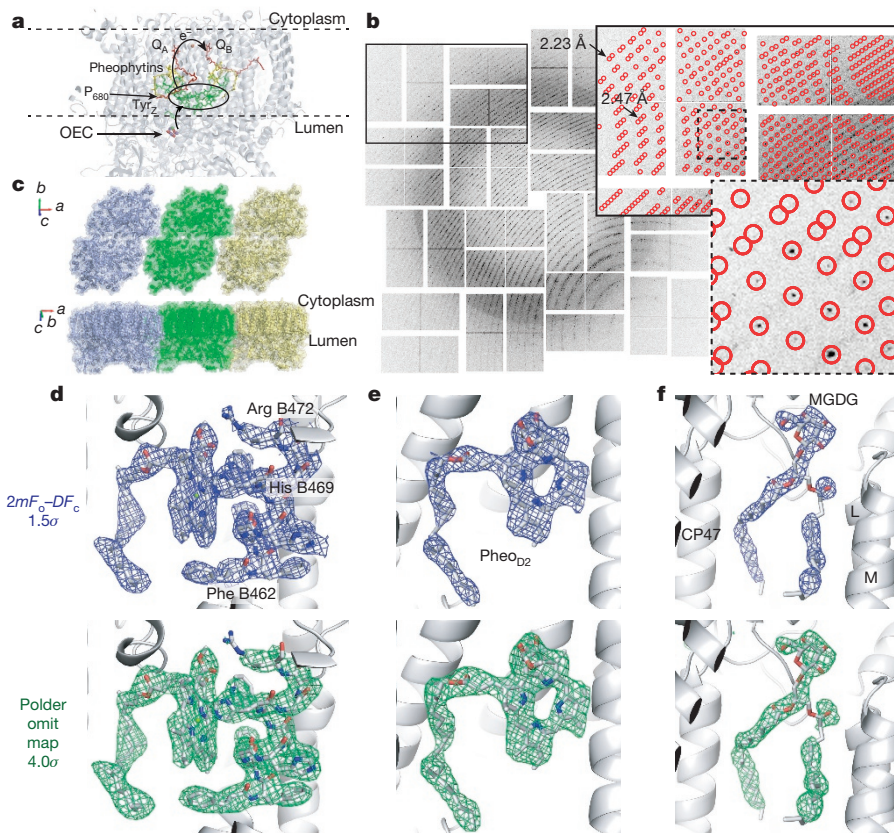


Figure 1 | Crystal structure of PS II in the dark (S_1) state collected at room temperature with femtosecond XFEL pulses. **a**, Schematic overview of the reaction centre of PS II showing cofactors involved in light-induced electron transfer and water oxidation. **b**, Diffraction pattern of a PS II microcrystal. Insets show enlarged views with the indexing solution. **c**, Arrangement of dimers in the unit cells of the crystals. Three

rates¹⁷ of about 25% and elongation of the distance between connecting chlorophylls of the antennae and reaction centre pigments from 20.5 to 20.9 Å yields a reduction in excitation transfer rates¹⁸ of about 10%.

The room temperature structure exhibits an increase of about 50% in altered rotamers of side-chains relative to the differences between the cryogenic XFEL and synchrotron radiation structures (Fig. 2d, e), indicating that the rotamer distribution is affected by temperature, as observed for other proteins⁸. These differences are observed nearly exclusively in solvent-exposed regions of the complex (Fig. 2d), and they can be explained by (a) high flexibility of the residues at room temperature leading to no or only weak electron density; (b) the presence of multiple conformers at room temperature (for example, Arg B476 in Fig. 2e); or (c) stabilization of a different conformer at room temperature (for example, Phe B479 in Fig. 2e).

In our room temperature S_1 and 2F- NH_3 XFEL structures (3.0 and 2.8 Å resolution, respectively), around 120 waters per dimer were resolved, with omit maps indicating the presence of additional waters (Methods, Extended Data Fig. 5 and Supplementary Table 6). In the higher-resolution native 2F room temperature XFEL structure, ~1,200 waters were observed. The observation of key water molecules linking the OEC to possible proton channels¹⁹ in our data (Extended Data Fig. 5) indicates that the channels postulated based on cryogenic structures^{7,19} may be relevant in PS II under physiological conditions.

Electron density maps for the OEC are shown in Fig. 3a, b and Extended Data Fig. 6 for the S_1 (3.0 Å) and 2F data (2.25 Å). To minimize model bias, metal–metal distances in the OEC (Fig. 3c) were calculated from individual metal omit maps. The similarity between the distances in the S_1 room temperature structure and those in the cryogenic S_1 XFEL structure⁷ (see error estimates in Methods) confirms that the observed metal arrangement at 100 K⁷ is valid for the

dimers (blue, green, yellow) with the view onto the membrane plane from the luminal side (top) and with the view along the membrane plane (bottom). **d–f**, Examples of omit maps with the model (grey). **d**, TMH 6 of CP47 with a Chl. **e**, Pheophytin in subunit D2. **f**, Monogalactosyl diacylglycerol (MGDG) lipid next to CP47.

physiological S_1 state at room temperature. Although it is difficult to determine bridging oxygen positions in multimetallic clusters such as the OEC, because the electron density of the oxygens tends to be overwhelmed by the nearby metal density, oxygen positions modelled in the room temperature S_1 state match well with those of the cryogenic S_1 XFEL structure. On the basis of the Mn4–O5 (~2.3 Å) and Mn1–O5 (~2.7 Å) distances, however, we concluded, as suggested by X-ray spectroscopy³, electron paramagnetic resonance (EPR)²⁰ and theory²¹, that O5 (Fig. 3a) is bound to the Mn4 site, but not bound to Mn1 in the S_1 state. This leads to an open cubane structure for the Mn₄CaO₅ unit.

In situ illumination of dark-adapted crystals at room temperature led to the formation of 2F crystals in which the S_3 state was predominant (Methods and Extended Data Fig. 7). In the 2F room temperature XFEL data, the cluster maintains its overall structure (Fig. 3b, c and Extended Data Fig. 6b), but changes are observed in some of the atomic positions, such as those of O4 and Mn4. The Mn3–Mn4 distance is shortened by about 0.1 Å and there is a twist of the Mn3–O4–Mn4–O5 plane in relation to the Mn1–Mn2–Mn3 core structure (Fig. 3d). While a distance uncertainty of 0.10–0.15 Å remains at 2.25 Å resolution, the trend in metal–metal distance changes does not support S_3 models based on closed cube geometries²² (for example, Extended Data Fig. 8a,d) that require more than 0.5 Å elongation of Mn3–Mn4 or compression of Mn1–Mn3 distances. Similarly, our data do not support models in which a new water or hydroxo binds to Mn1^{20,21} (Extended Data Fig. 8b), as no corresponding electron density or distance changes were observed (Fig. 3e, f and Extended Data Fig. 6b).

All four water ligands to the OEC (W1–W4, Extended Data Fig. 1a) are clearly visible in our S_3 -enriched 2F room temperature XFEL data, within 0.2–0.4 Å of their positions in the cryogenic S_1 XFEL structure; for example, W3 is displaced towards Glu189 and W4 towards Asp170

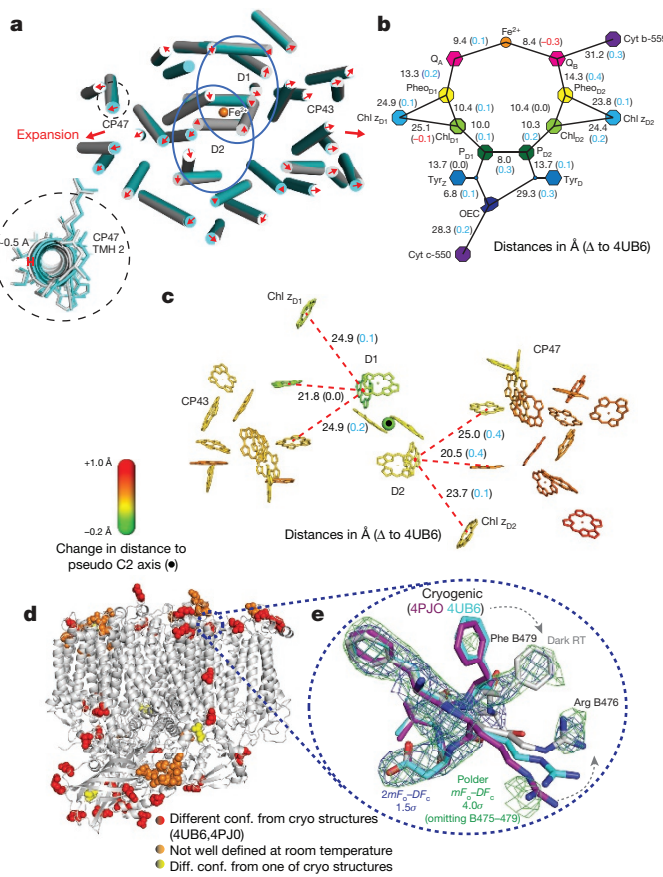


Figure 2 | Comparison of the room temperature and cryogenic structures in the dark state. **a**, Location of TMH in one monomer at room temperature (grey cylinders) and the cryogenic structure⁷ (cyan). View is onto the membrane plane from the cytoplasmic side. One TMH is shown enlarged in the inset to illustrate the shift between the cryogenic and room temperature structures. **b**, Distances between the cofactors of the electron transport chain in the dark structure, with differences from the cryogenic structure⁷ in parentheses. **c**, Changes in Chl-Pheo distances, represented by colour. **d**, Location of residues that show different side chain orientations at room temperature compared to the cryogenic structures^{7,16}. **e**, Examples of different side chain positions in the room temperature structure (grey) with the cryogenic structures (cyan⁷, purple¹⁶). Dashed lines indicate the location of these residues in the PS II complex.

(Fig. 3b, d and Extended Data Fig. 5e; note that the W3 position in our room temperature S₁ structure is shifted by about 0.8 Å from that of the cryogenic S₁ XFEL structure, Extended Data Fig. 5d). No additional water or hydroxo ligand to the OEC was observed in the 2F data. Comparison of the roughly 20 waters within 7 Å of the OEC indicated that three of the second-sphere waters from the cryogenic S₁ XFEL structure (A571, A588 and C665) could not be located in the 2F structure, probably owing to their mobility at room temperature or changes in the water arrangement around the OEC upon formation of the S₃ state (Extended Data Fig. 5e).

There are no large movements of the side chains surrounding the OEC—for example, Asp 61, Asp 170 and Val 185 of D1—between the dark and native 2F structures (Fig. 3a, b, d) of the sort predicted in previous studies^{14,23}. Instead, small movements on the order of 0.3 Å are noticeable in several side chains, in agreement with the data from ref. 24.

At the electron-acceptor site, no large differences are observed for the mobile quinone Q_B between the dark and native 2F structures. This is in line with the expectation that after two flashes Q_BH₂ is released and the Q_B pocket is filled with a new plastoquinone within the 500 ms period before sampling with the XFEL pulse (Extended Data Fig. 7a, b).

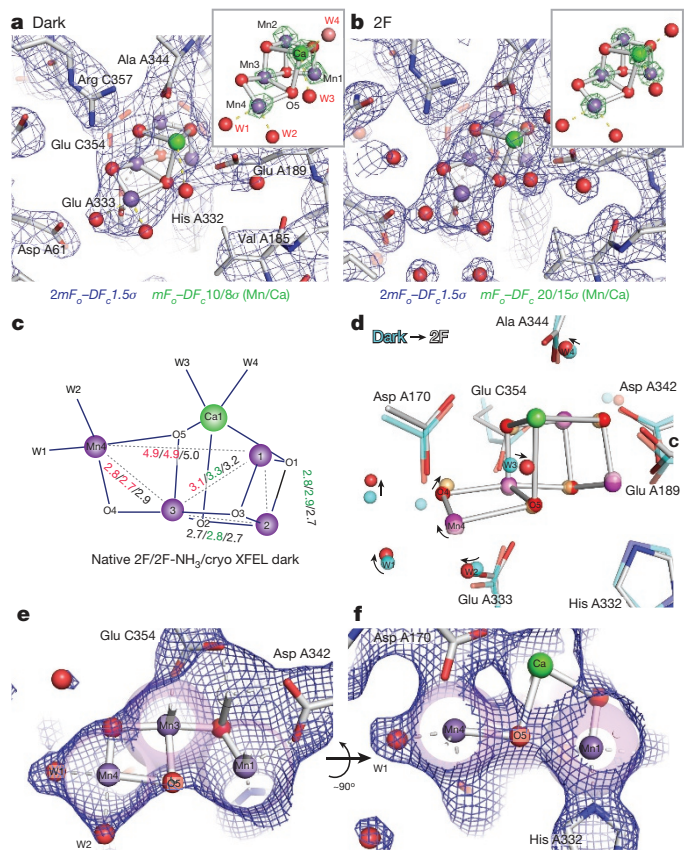


Figure 3 | The oxygen evolving complex. **a, b**, Electron density around the OEC of the dark (a) and 2F (b) room temperature structures. Insets, individual metal atom omit maps. **c**, Mn–Mn distances obtained from metal omit maps for the 2F and 2F-NH₃ data compared with the distances from ref. 7. **d**, Perturbations in the vicinity of the Mn₄CaO₅ cluster in the 2F state (grey) in comparison to ref. 7 (cyan). **e, f**, Electron density in the Mn1–O5–Mn4 region in two different orientations. Density (blue mesh, half the grid spacing compared to other maps shown) is contoured at 1.8σ, matching the van der Waals radius (light magenta spheres) of Mn. Clear density protruding beyond the van der Waals volume of the Mn is visible for metal bound waters (for example, W1, W2) but no extra density is seen around Mn1, a proposed location of an inserted water in the Mn₄CaO₅ cluster in the S₃ state.

Insight into which of the water or hydroxo ligands of the Mn₄CaO₅ cluster are the substrate waters can be obtained by analysing differences induced by ammonia binding (see Supplementary Information). Ammonia is known to bind to the Mn₄CaO₅ cluster at a non-substrate water binding site only upon illumination¹⁰. We therefore obtained 2F room temperature XFEL data at pH 7.5 (2F-NH₃, 2.8 Å resolution) in the presence of 100 mM (NH₄)₂SO₄, and compared it with the native 2F data. In the 2F-NH₃ structure, about 75% of PS II centres are in either the S₂ or S₃ state (Methods and Extended Data Fig. 7f–i). Binding of ammonia to Mn was confirmed by the altered S₂ EPR multiline signal²⁵ (Extended Data Fig. 7d, e). Although the Cl[−]-binding site was reported as a second, possibly inhibitory ammonia-binding site (see Supplementary Information), we can exclude substitution of Cl[−] by ammonia in our samples based on oxygen-evolution activity (Extended Data Fig. 7f–i) and inspection of the electron density (Extended Data Fig. 9a, b). As a direct distinction between NH₃ and H₂O cannot be drawn from the data, we examined the structure around possible binding sites in the 2F-NH₃ data in comparison with the native 2F structure.

One of the proposed ammonia-binding sites is the μ-oxo bridging ligand O5 (Fig. 4A). Elongation of the Mn3–Mn4 distance is expected upon replacement of a μ-oxo bridge with an amido or imido-bridge¹¹ or a significant alteration of the core structure²⁶; for example, changing

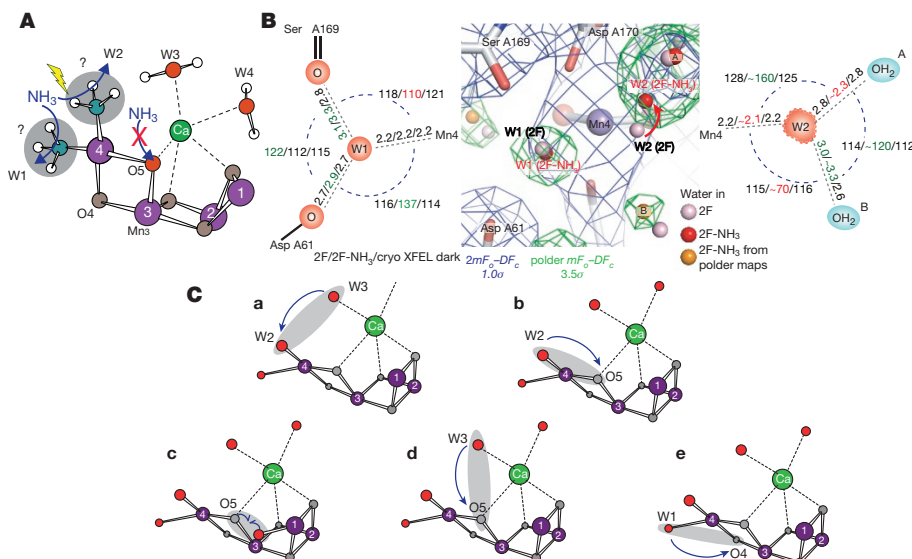


Figure 4 | Ammonia binding sites to the OEC and O–O bond formation mechanisms. **A**, Schematic of the OEC showing suggested locations of ammonia binding upon illumination. **B**, Electron density in the vicinity of Mn4, showing waters W1 and W2 and their surroundings in the 2F and 2F-NH₃ data. Left, Schematic of the bonding geometry of W1 and W2 in ref. 7; right, the 2F and 2F-NH₃ room temperature structures; note that the 2F-NH₃ W2 position is not well defined and angles and distances are

from a di- μ -oxo to a mono- μ -oxo interaction upon loss of the Mn3–O5–Mn4 μ -oxo bridge. No such elongation was observed in the 2F-NH₃ data and therefore we eliminate this possibility, in agreement with EPR data¹². Alternatively, ammonia could replace a terminal water ligand on Mn4 (W1 or W2; Fig. 4A), with W1 being favoured based on the interpretation of EPR data^{12,13}. The W1 position in the 2F-NH₃ data is very similar to that in the native 2F structure, while the placement of W2 reveals a shift of its position (Fig. 4B and Extended Data Fig. 9). Of the waters hydrogen-bonded to W2, H₂O^A (Fig. 4B) is in a position similar to that in the native 2F and cryogenic S₁ XFEL structures, whereas H₂O^B is less well defined. A larger tilt of the W3 and W4 axis is also visible in the 2F-NH₃ data as compared with the native 2F data. We note that the native 2F data were obtained by lowering the pH from 7.5 to 6.5; thus, an alternative explanation for the observed change in the W2 site is that W2 is a hydroxide at pH 7.5, while it is fully protonated at pH 6.5.

Modelling the binding of NH₃ in place of W1 in the S₂-state^{12,27} predicted either changes in the Mn3–Mn4 distance by 0.4 Å and displacement of the ammonia nitrogen with respect to the W1 position by about 1 Å²⁷ or ammonia at a position very similar to W1 in the structure shown in ref. 7 with minimal changes in the Mn3–Mn4 distance and a small movement of W2¹². As our data do not show elongation of the Mn3–Mn4 distance, a scenario as postulated in ref. 27 is unlikely. This leaves two options for NH₃-binding in the S₃ state, either at W1 with only minimal changes in the metal positions and ligand environment or at W2 (Fig. 4A).

W2 is less integrated than W1 in a strong hydrogen-bonding network (as also seen in ref. 7), suggesting that there will be easier exchange of W2 if it is bound as fully protonated H₂O. On the other hand, the weaker H-bonding makes ammonia binding at the W2 site difficult to reconcile with the highly anisotropic nuclear quadrupole parameter of the bound ammonia¹³. We note that our data do not exclude ammonia moving from the W1 to W2 site or detaching from Mn during the S₂ → S₃ transition^{27,28}.

Ammonia binding does not significantly affect the substrate water exchange rates in the S₂ and S₃ states^{10,12} (Extended Data Fig. 7). Therefore, if the structural change at W2 is caused, directly or indirectly, by ammonia binding, then W2 is not a likely substrate binding site in

only approximations. **C**, Proposed O–O bond formation mechanisms. **Ca**, Water-nucleophilic attack of Ca-bound W3 onto W2 (for example, Mn(V)-oxo in S₄); **Cb**, coupling between W2 and O5; **Cc**, oxo-oxyl radical coupling mechanism between a hydroxyl in the S₂ → S₃ transition (hydroxyl in S₄) to Mn1 and the O5-bridge; **Cd**, nucleophilic attack of Ca-bound W3 onto O5; **Ce**, oxo-oxyl coupling between W1 and O4.

the S₃-state. In the context of the proposed mechanisms^{4,29–31} (Fig. 4C), this would disfavour O–O bond formation via nucleophilic attack from Ca-bound W3 onto W2 (Fig. 4C, a) and other mechanisms that use W2 (for example, Fig. 4C, b). As we did not find evidence for the presence of an additional water or hydroxyl near Mn1 in the 2F samples, our data do not support direct coupling between a newly bound water-derived ligand in the S₃ state on Mn1 and O5 (Fig. 4C, c; see also ref. 2). This will leave possible mechanisms such as O–O bond formation between W3 and O5 (Fig. 4C, d), between W1 and O4 (Fig. 4C, e), or other relevant mechanisms.

Online Content Methods, along with any additional Extended Data display items and Source Data, are available in the online version of the paper; references unique to these sections appear only in the online paper.

Received 10 June; accepted 14 October 2016.

Published online 21 November 2016.

- Kok, B., Forbush, B. & McGloin, M. Cooperation of charges in photosynthetic O₂ evolution-I. A linear four step mechanism. *Photochem. Photobiol.* **11**, 457–475 (1970).
- Cox, N. & Messinger, J. Reflections on substrate water and dioxygen formation. *Biochim. Biophys. Acta* **1827**, 1020–1030 (2013).
- Yano, J. & Yachandra, V. Mn₄Ca cluster in photosynthesis: where and how water is oxidized to dioxygen. *Chem. Rev.* **114**, 4175–4205 (2014).
- Messinger, J., Badger, M. & Wydrzynski, T. Detection of one slowly exchanging substrate water molecule in the S₃ state of photosystem II. *Proc. Natl. Acad. Sci. USA* **92**, 3209–3213 (1995).
- Hillier, W. & Wydrzynski, T. ¹⁸O-Water exchange in photosystem II: Substrate binding and intermediates of the water splitting cycle. *Coord. Chem. Rev.* **252**, 306–317 (2008).
- Ugur, I., Rutherford, A. W. & Kaila, V. R. Redox-coupled substrate water reorganization in the active site of photosystem II-The role of calcium in substrate water delivery. *Biochim. Biophys. Acta* **1857**, 740–748 (2016).
- Suga, M. et al. Native structure of photosystem II at 1.95 Å resolution viewed by femtosecond X-ray pulses. *Nature* **517**, 99–103 (2015).
- Fraser, J. S. et al. Accessing protein conformational ensembles using room-temperature X-ray crystallography. *Proc. Natl. Acad. Sci. USA* **108**, 16247–16252 (2011).
- Tilton, R. F., Jr, Dewan, J. C. & Petsko, G. A. Effects of temperature on protein structure and dynamics: X-ray crystallographic studies of the protein ribonuclease-A at nine different temperatures from 98 to 320 K. *Biochemistry* **31**, 2469–2481 (1992).
- Boussac, A., Rutherford, A. W. & Styring, S. Interaction of ammonia with the water splitting enzyme of photosystem II. *Biochemistry* **29**, 24–32 (1990).

11. Britt, R. D., Zimmermann, J. L., Sauer, K. & Klein, M. P. The state of manganese in the photosynthetic apparatus. 10. Ammonia binds to the catalytic Mn of the oxygen-evolving complex of photosystem-II - evidence by electron-spin echo envelope modulation spectroscopy. *J. Am. Chem. Soc.* **111**, 3522–3532 (1989).
 12. Pérez Navarro, M. et al. Ammonia binding to the oxygen-evolving complex of photosystem II identifies the solvent-exchangeable oxygen bridge (μ -oxo) of the manganese tetramer. *Proc. Natl. Acad. Sci. USA* **110**, 15561–15566 (2013).
 13. Oyala, P. H., Stich, T. A., Debus, R. J. & Britt, R. D. Ammonia binds to the dangler manganese of the photosystem II oxygen-evolving complex. *J. Am. Chem. Soc.* **137**, 8829–8837 (2015).
 14. Kupitz, C. et al. Serial time-resolved crystallography of photosystem II using a femtosecond X-ray laser. *Nature* **513**, 261–265 (2014).
 15. Sauter, N. K. et al. No observable conformational changes in PSII. *Nature* **533**, E1–E2 (2016).
 16. Hellmich, J. et al. Native-like photosystem II superstructure at 2.44 Å resolution through detergent extraction from the protein crystal. *Structure* **22**, 1607–1615 (2014).
 17. Moser, C. C., Keske, J. M., Warncke, K., Farid, R. S. & Dutton, P. L. Nature of biological electron transfer. *Nature* **355**, 796–802 (1992).
 18. Förster, T. Zwischenmolekulare Energiewanderung und Fluoreszenz. *Ann. Phys.* **437**, 55–75 (1948).
 19. Umena, Y., Kawakami, K., Shen, J.-R. & Kamiya, N. Crystal structure of oxygen-evolving photosystem II at a resolution of 1.9 Å. *Nature* **473**, 55–60 (2011).
 20. Cox, N. et al. Electronic structure of the oxygen-evolving complex in photosystem II prior to O–O bond formation. *Science* **345**, 804–808 (2014).
 21. Siegbahn, P. E. M. Structures and energetics for O₂ formation in photosystem II. *Acc. Chem. Res.* **42**, 1871–1880 (2009).
 22. Glöckner, C. et al. Structural changes of the oxygen-evolving complex in photosystem II during the catalytic cycle. *J. Biol. Chem.* **288**, 22607–22620 (2013).
 23. Li, X. & Siegbahn, P. E. M. Alternative mechanisms for O₂ release and O–O bond formation in the oxygen evolving complex of photosystem II. *Phys. Chem. Chem. Phys.* **17**, 12168–12174 (2015).
 24. Kern, J. et al. Taking snapshots of photosynthetic water oxidation using femtosecond X-ray diffraction and spectroscopy. *Nat. Commun.* **5**, 4371 (2014).
 25. Beck, W. F., Depaula, J. C. & Brudvig, G. W. Ammonia binds to the manganese site of the O₂-evolving complex of photosystem II in the S₂ state. *J. Am. Chem. Soc.* **108**, 4018–4022 (1986).
 26. Hou, L. H., Wu, C. M., Huang, H. H. & Chu, H. A. Effects of ammonia on the structure of the oxygen-evolving complex in photosystem II as revealed by light-induced FTIR difference spectroscopy. *Biochemistry* **50**, 9248–9254 (2011).
 27. Askerka, M., Vinyard, D. J., Brudvig, G. W. & Batista, V. S. NH₃ binding to the S₂ state of the O₂-evolving complex of photosystem II: Analogue to H₂O binding during the S₂ → S₃ transition. *Biochemistry* **54**, 5783–5786 (2015).
 28. Retegan, M. et al. A five-coordinate Mn(IV) intermediate in biological water oxidation: spectroscopic signature and a pivot mechanism for water binding. *Chem. Sci. (Camb.)* **7**, 72–84 (2016).
 29. Pecoraro, V. L., Baldwin, M. J., Caudle, M. T., Hsieh, W. Y. & Law, N. A. A proposal for water oxidation in photosystem II. *Pure Appl. Chem.* **70**, 925–929 (1998).
 30. Vrettos, J. S., Limburg, J. & Brudvig, G. W. Mechanism of photosynthetic water oxidation: combining biophysical studies of photosystem II with inorganic model chemistry. *Biochim. Biophys. Acta* **1503**, 229–245 (2001).
 31. Yamanaka, S. et al. Possible mechanisms for the O–O bond formation in oxygen evolution reaction at the CaMn₄O₅(H₂O)₄ cluster of PSII refined to 1.9 Å X-ray resolution. *Chem. Phys. Lett.* **511**, 138–145 (2011).
- Supplementary Information** is available in the online version of the paper.
- Acknowledgements** This work was supported by the Director, Office of Science, Office of Basic Energy Sciences (OBES), Division of Chemical Sciences, Geosciences, and Biosciences (CSGB) of the Department of Energy (DOE) (J.Y., V.K.Y.) for X-ray methodology and instrumentation; National Institutes of Health (NIH) grants GM055302 (V.K.Y.) for PS II biochemistry, structure and mechanism, GM110501 (J.Y.) for instrumentation development for XFEL experiments, GM102520 and GM117126 (N.K.S.) for development of computational protocols for XFEL data; the Ruth L. Kirschstein National Research Service Award (GM116423-02, F.D.F.); and the Human Frontiers Science Project Award No. RGP0063/2013 310 (J.Y., U.B., P.W., A.Z.). The DFG-Cluster of Excellence “UniCat” coordinated by T.U. Berlin and Sfb1078 (Humboldt Universität Berlin), TP A5 (A.Z., H.D.), the Solar Fuels Strong Research Environment (Umeå University), the Artificial Leaf Project (K&A Wallenberg Foundation 2011.0055) and Energimyndigheten (36648-1) (J.M.) are acknowledged for support. H.L. and C.A.S. acknowledge support from the US DOE, OBES, CSGB Division, W.I.W. and A.T.B. acknowledge support from an HHMI Collaborative Innovation Award. D.G.W. is funded by industrial income received by CCP4. This research used resources of NERSC, a User Facility supported by the Office of Science, DOE, under Contract No. DE-AC02-05CH11231. Portions of this work were supported by a BNL/US DOE, LDRD grant (11-008; A.M.O.); and NIH/NIGMS grant 2-P41-RR012408, NIH/NIGMS grants 8P41GM103473-16 and P41GM111244 and the US DOE, OBER grant FWP BO-70 (A.M.O., B.A.). A.M.O and P.T.D were supported in part by the Diamond Light Source, and A.M.O acknowledges support from a Strategic Award from the Wellcome Trust and the Biotechnology and Biological Sciences Research Council (grant 102593). P.B. was supported by a Wellcome Trust DPhil studentship. Testing of crystals and various parts of the setup were carried out at synchrotron facilities that were provided by the Advanced Light Source (ALS) in Berkeley and Stanford Synchrotron Radiation Lightsource (SSRL) in Stanford, funded by DOE OBES under contract DE-AC02-05CH11231 (ALS) and DE-AC02-76SF00515 (SSRL). The SSRL Structural Molecular Biology Program is supported by the DOE OBER and by the NIH (P41GM103393). Use of the LCLS and SSRL, SLAC National Accelerator Laboratory, is supported by the US DOE, Office of Science, OBES under Contract No. DE-AC02-76SF00515. We thank M. Bommer for discussions and help regarding structure refinement, crystallographic model building and validation, J. Hattne for his contributions to the development of XFEL diffraction data processing, A. Boussac for discussions on ammonia binding and his contributions to the substrate water exchange measurements of the S₃ state in the presence of ammonia, and the previous CXI beamline scientist, G. Williams, for his support during the initial stages of this project. We thank the support staff at LCLS/SLAC and at SSRL (BL 6-2, 7-3) and ALS (BL 5.01, 5.0.2, 8.2.1).
- Author Contributions** U.B., V.K.Y. and J.Y. conceived the experiment; R.A.-M., S.B., A.Z., J.M., U.B., N.K.S., J.K., V.K.Y. and J.Y. designed the experiment; I.D.Y., M.I., R.C., R.T., M.A.B., R.H., M.Z., L.D., I.S., A.Z. and J.K. prepared samples; M.S.H., A.A., J.E.K., J.R., M.L. and S.B. operated the CXI instrument; R.A.-M., T.J.L., J.E.K., J.R., M.L. and S.B. operated the MFX instrument; R.A.-M., J.M.G., S.N., M.S. and D.Z. operated the XPP instrument; S.G., S.K., F.D.F., H.L., E.P., B.A., A.M.O., R.G.S., C.A.S., C.S., J.M. and J.K. developed, tested and ran the sample delivery system; R.C., S.K., C.d.L., L.V.P., H.N., M.H.C., D.S.H., J.M. and J.Y. performed and analysed O₂ evolution and EPR measurements; I.D.Y., M.I., R.C., S.G., S.K., A.S.B., R.A.-M., F.D.F., T.K., T.M.-C., H.L., R.G.S., C.A.S., R.H., M.Z., L.D., M.K., C.d.L., C.S., D.So., T.-C.W., E.P., C.W., T.F., P.A., P.B., B.A., P.T.D., A.M.O., J.M.G., S.N., M.S., D.Z., M.S.H., T.J.L., A.A., J.E.K., J.R., M.L., S.B., P.W., A.Z., J.M., U.B., N.K.S., J.K., V.K.Y. and J.Y. performed the LCLS experiment; I.D.Y., A.S.B., T.M.-C., A.Y.L., M.U., N.W.M., D.L., P.V.A., D.G.W., G.E., W.I.W., A.T.B., P.H.Z., P.D.A. and N.K.S. developed new software for data processing; I.D.Y., A.S.B., F.D.F., C.W., T.F., LL, P.A., P.B., T.K., T.M.-C., H.D., N.K.S. and J.K. processed and analysed XFEL data; I.D.Y., R.C., J.M., J.K., J.Y. and V.K.Y. wrote the manuscript with input from all authors.
- Author Information** Reprints and permissions information is available at www.nature.com/reprints. The authors declare no competing financial interests. Readers are welcome to comment on the online version of the paper. Correspondence and requests for materials should be addressed to A.Z. (athina.zouni@hu-berlin.de), J.M. (johannes.messinger@umu.se), V.K.Y. (vkyachandra@lbl.gov) or J.Y. (jyano@lbl.gov).
- Reviewer Information** *Nature* thanks J. Murray, C. Yocom and the other anonymous reviewer(s) for their contribution to the peer review of this work.

METHODS

Sample preparation. PS II dimers from *Thermosynechococcus (T.) elongatus* were prepared using a modification of the protocol described in ref. 32, substituting the C₁₂E₈ detergent for β-DM and using betaine as a cryoprotectant instead of glycerol¹⁶. Crystallization was achieved by addition of PEG 5000 and seeding methods³³ to obtain a uniform size distribution of 5–15 μm for the MESH (microfluidic electrokinetic sample holder) injector (CXI instrument at LCLS) and 20–50 μm for the ADE (acoustic droplet ejection)-DOT (droplet on tape) injector (XPP and MFX instruments at LCLS) (see Sample Injection and Illumination). Crystals were dehydrated by treatment with high concentrations of PEG 5000 before measurement. The final buffer used for the XRD measurements for the CXI instrument was 100 mM TRIS-Cl, pH 7.5, 100 mM (NH₄)₂SO₄, 31.5% (w/v) PEG 5000, 10% ethylene glycol. This procedure resulted in a change in unit cell parameters of the crystals compared to earlier crystallization protocols due to differences in crystal packing. The packing obtained from this procedure¹⁶ is very similar to the arrangement of PS II dimers in the native thylakoid membrane of *T. elongatus*. The final buffer used for the XRD measurements for the XPP and MFX instruments was 100 mM MES pH 6.5, 100 mM ammonium chloride, 10% ethylene glycol and 35% (w/v) PEG 5000. Crystalline unit cells for structures determined at the CXI instrument (S₁ and 2F-NH₃) differed from the one determined at the XPP and MFX instruments (2F), particularly in the *c*-axis dimension (Extended Data Table 1). The differences in the unit cell parameters are due to the different buffer conditions and dehydration procedures. Nevertheless, a similar dimer–dimer interaction in the direction of the membrane plane was observed in both crystal forms.

Characterization of ammonia-treated PS II and establishing the preparation protocol. Prolonged incubation of PS II samples at higher pH, and with ammonia and TRIS, are known to reduce the PS II oxygen evolution activity. For this reason, thorough control experiments were undertaken to characterize the light-induced turnover of purified PS II dimers under crystallization conditions in comparison to conditions at lower pH and without ammonia or TRIS addition. The buffers used were A (100 mM MES, pH 6.0, 10 mM CaCl₂, 30% glycerol) for low pH conditions, B (100 mM TRIS-Cl, pH 7.5, 100 mM (NH₄)₂SO₄, 30% glycerol) to mimic crystallization conditions in solution samples, C (100 mM TRIS-Cl, pH 7.5, 100 mM (NH₄)₂SO₄, 31.5% PEG 5000, 10% ethylene glycol) for measurements on crystals and D (100 mM TRIS-Cl, pH 7.5, 10 mM CaCl₂, 30% glycerol) for measurements at high pH without ammonia. EPR measurement of the content of Mn²⁺ released from crystals after 12 h incubation in buffer C yielded an upper bound of 5%.

O₂ activity. Measurement of the O₂ yield by means of a Clark-type electrode from ammonia-treated crystals under continuous illumination showed 70–75% of the activity observed under low pH conditions (pH 6.0). To see whether this reduction in activity is due to the pH effect or to some fraction of Cl[−] binding sites being substituted with ammonia, we compared the O₂ activity of PS II in buffer A (pH 6.0, no ammonia), in buffer B (pH 7.5 with ammonia), and in buffer D (pH 7.5, CaCl₂, no ammonia). The O₂ evolution rates of PS II in buffer B and in buffer D were similar and were 70% of the activity in buffer A (~3,000 μmol O₂/(mg(Chl) × h)) with PPBQ and 3,600 μmol O₂/(mg(Chl) × h) with DCBQ). Therefore, we conclude that the reduction in the O₂ activity in our ammonia-treated PS II is an effect of the higher pH, not of the displacement of chloride. Similar results were obtained by Joliot-type O₂ evolution measurements (no electron acceptors added, 2 Hz flash frequency, Xe-flash lamp) on the same type of PS II core preparations (Extended Data Fig. 7f–i). These experiments revealed a similar O₂ oscillation pattern and comparable total O₂ yields with and without ammonia or TRIS or MOPS buffer at pH 7.5, even if incubated for several hours. One exception was that the total O₂ yield of the sample in buffer containing 100 mM (NH₄)₂SO₄ was 30% smaller than when suspended in buffer containing 100 mM Na₂SO₄. The data also show that our core preparations have a large enough plastoquinone pool to allow a full cycle of O₂ production in the absence of added electron acceptors (Extended Data Fig. 7a). This was further confirmed by membrane-inlet mass spectrometry experiments in which at very low frequency (12 s between flashes) an increase in O₂ yield of only 15% was observed if PPBQ was added (Extended Data Fig. 7b). The experiments were performed and analysed as described earlier³⁴.

Importantly, nearly full activity (O₂ rates) can be restored in solution samples by exchanging the sample back into pH 6.5 buffer, but keeping the (NH₄)₂SO₄ concentration constant. This implies that the OEC remains intact and that the lower overall activity at the higher pH may be associated with changes in the protonation state of residues involved in proton transfer networks around the OEC.

Electron density of the Cl[−] binding site. As described above, ammonia does not bind to the Cl[−] binding site(s) in the presence of excess Cl[−] (100 mM) in PS II, and the O₂ activity results support this conclusion. To further confirm this, we checked the occupation of the two Cl[−] binding sites in the electron density map of the 2F data. As shown in Extended Data Fig. 9a, b, both sites are occupied by chloride. We have also checked this by substituting chloride with ammonia in the

structural model and calculating electron density difference maps using this substituted model after three cycles of refinement in *phenix.refine*. The appearance of positive difference density upon substitution confirmed that the density observed at both chloride-binding sites in the electron density maps from our dark and 2F data cannot be explained by ammonia (Extended Data Fig. 9 a, b). In summary, we can conclude that ammonia does not bind to the chloride-binding sites under the current experimental conditions.

EPR spectra of ammonia-treated PS II. Previous studies have suggested that ammonia binds upon formation of the S₂-state and stays bound in the S₂–S₃ transition¹⁰. Therefore, we used the well-characterized S₂ EPR multiline signal (MLS) to infer the extent of ammonia binding in our 2F samples. The binding of ammonia to Mn in the S₂-state was confirmed by the altered EPR multiline spectrum. We measured EPR from both single flash (data not shown) and continuous illumination conditions with and without annealing to populate the S₂-state. These different procedures yielded similar results and for comparison with published data we show here the spectra obtained using continuous illumination and annealing (Extended Data Fig. 7d, e). We compared the native PS II EPR multiline spectrum of the S₂-state (pH 6.0, no ammonia), the native PS II EPR multiline spectrum of the S₂-state (pH 7.5, no ammonia), and the ammonia-treated S₂-state spectrum (pH 7.5 in the presence of 100 mM ammonia). The spectral changes observed in the ammonia-treated S₂-state sample were similar to results reported previously^{13,35} and the altered MLS was observed. Comparing spectral heights between the altered and native MLS is challenging as the peaks do not clearly correspond to each other. Nevertheless, when we assume that the MLS intensity of normal PS II (pH 7.5 without ammonia) and the altered MLS of ammonia-bound PS II (pH 7.5 with ammonia) both similarly reflect the number of unpaired spins, we estimate the altered (ammonia-treated) MLS intensity to be ~70% of that of the non-ammonia-treated PS II (calculated by the averaged peak heights of multiple EPR peaks at the high field side of the Y_D signal). The reduction in the MLS gives a lower limit of 70% for centres in the S₂-state as it could also be that, under elevated pH conditions, a fraction of the centres in the S₂ state do not give an MLS³⁶.

Determination of the S₃ state population in the native and ammonia-treated PS II 2F states. Flash-induced oxygen measurements in a replica of the capillary setup used in the XRD experiment were performed using membrane inlet mass spectrometry (MIMS) for O₂ detection^{24,37,38}. Analysis of the flash data obtained for PS II crystals incubated for 12 h in buffer C (Extended Data Fig. 7f) showed that 50–60% of the centres that are active in oxygen evolution are in the S₃-state after two light flashes in the ammonia-treated PS II. We therefore conclude that in the 2F ammonia-treated PS II samples, S₃ is formed in 50–60% of the centres, with most of the remaining centres (~25%) being in the S₂-state. Therefore, 75–85% of the centres are expected to bind ammonia in the 2F samples. This estimate was confirmed with the independent Joliot-type flash-induced oxygen evolution measurements on solution samples of our PS II core complexes. The analysis of these patterns (Extended Data Fig. 7 g–i) gives a S₃ state population of about 53% in the 2F samples at pH 7.5 (TRIS, (NH₄)₂SO₄), and of 60% at pH 6.5 (MES, (NH₄)₂SO₄) (Extended Data Fig. 7a, g–i).

At pH 7.5, the O₂ evolution rate is reversibly reduced to 70–75% of its maximum value at pH 6.0, and the MLS amplitude is reduced to a similar extent (Extended Data Fig. 7d). Similarly, the total O₂ yield obtained in the flash-induced oxygen evolution pattern was about 50% at pH 7.6 compared to pH 6.5. As we do not know with certainty whether these reductions are due to reversible blockage of centres in a particular S-state or due to kinetic limitations (O₂) or changes in the hyperfine couplings (EPR)³⁶, some uncertainty arises as to the S-state population of the 2F-NH₃ samples when normalized to all centres. Therefore, the most conservative estimate for the S-state distribution in the current 2F-NH₃ crystals is 25% S₃-state. In contrast, the highest estimate of the S₃-state occupancy in the 2F-NH₃ sample becomes 50%, with 25% in the S₂-state.

Sample injection and illumination. Crystals in high PEG 5000 buffer (31.5% w/v) were injected using a modified version of the electrospinning injector (MESH) from ref. 39. In the modified version, a double capillary setup was used, allowing the protection of the crystals in mother liquor with a shield flow of 50% ethylene glycol. The setup is discussed in detail in ref. 40. Illumination of samples was performed as described previously²⁴ and optimal illumination parameters were established by parallel oxygen yield measurements using MIMS (Extended Data Fig. 7b, c, f). The experimental setup at the CXI instrument^{41,42} of LCLS was similar to the one used in our previous work^{24,43}. For the ammonia-treated doubly illuminated (2F-NH₃) data, each volume segment of the crystal suspension was illuminated by 120-ns laser pulses (20 ± 2 mJ/cm²) at 527 nm from lasers 2 and 3 along the sample delivery capillary, resulting in a delay time of 0.5 s between the first and second illuminations and of 0.5 s between the second illumination and the X-ray probe.

For the high-resolution 2F structure of the native PS II, the data were collected at the XPP⁴⁴ and the MFX⁴⁵ instruments of LCLS. The newly developed DOT sample

delivery method was used in combination with an ADE method (Fuller, F. D. *et al.*, submitted). The laser illumination timing remains the same as that used for MESH with the difference of 1 s spacing between first and second fibre excitations and between the last fibre excitation and the X-ray probe, using 100-ns laser pulses at 527 nm from a Nd:YLF laser (Evolution, Coherent). To test light saturation for the DOT system, a 100–150- μm film was established with the help of a washer between the silicon membrane of the mass spectrometer inlet and a thin microscope glass plate (thin layer MIMS setup). In this test setup the samples were illuminated with a pulsed Nd:YAG laser (532 nm, Continuum). The laser energy was measured at the sample position. To allow resolution of the individual O₂ yields (Y_n ; n = flash number), the flashes had to be spaced by 12 s, which leads to a significantly lower Y3/Y4 ratio (Extended Data Fig. 7b) than at 1 or 2 Hz as used in the Joliot-type experiments (Extended data Fig. 7a, g–i) and during the XFEL measurements. The data in Extended Data Fig. 7c show that the samples are saturated at 70 mJ/cm². At the XFEL a light intensity of $120 \pm 10 \text{ mJ/cm}^2$ was applied.

X-ray diffraction setup and data processing. PS II XRD data collected at the CXI instrument^{41,42} of LCLS were recorded on a CSPAD detector⁴⁶ operating at a frame rate of 120 Hz over an aggregate total time period of 641 min and processed using *cctbx.xfel*^{47,48}. To avoid saturating pixels on the CSPAD, which has a limited dynamic range of ~ 350 photons per pixel at 8 keV in its high gain mode⁴⁶, we used the CSPAD detector in a mixed gain mode, putting the low resolution pixels in a low-gain setting while the high resolution pixels were set to high gain. The low-gain mode is less sensitive to low signal but harder to saturate, thus preserving bright, low resolution reflections. Conversely, the high-gain setting is easier to saturate, but is more sensitive to low signal, as is typical for high resolution reflections. After subtracting a pedestal estimate derived from an uncorrected, dark average, we applied a gain multiplier of 6.88 to the pixels in the low-gain setting, thereby putting low- and high-gain pixels on a similar scale. This number is merely an estimate based on matching the background levels at the low–high gain boundary. A more thorough exploration of gain for protein diffraction data on the CSPAD detector is planned.

Thermolysin pseudo-powder patterns were generated by taking the maximum value of each pixel from the ensemble of diffraction patterns in a reference thermolysin dataset⁴⁰ collected at a known detector distance. A precise sample-to-detector distance and the locations and orientations of the 64 sensors on the CSPAD X-ray diffraction detector were obtained by refining the geometries of the 64 sensors against all the single crystal models from the dataset⁴⁸.

PS II XRD data collected at the XPP⁴⁴ and the MXF⁴⁵ instruments were recorded on a Rayonix MX170-HS detector operating at its maximum frame rate of 10 Hz in the 2-by-2 binning mode, in which square bins of four pixels are configured to share underlying electronics and act as a single pixel. This mode was selected as a compromise between high data acquisition rates at larger effective pixel sizes and improved ability to resolve individual Bragg spots, especially for large unit cells, at smaller effective pixel sizes. In all binning modes, the dynamic range of the Rayonix detector is also larger than that of the CSPAD. Using this detector and the ADE–DOT sample delivery system, XRD data could be acquired from larger crystals (20–50 μm) than were used at the CXI instrument using the CSPAD and the modified MESH sample delivery system (5–15 μm).

Images were indexed using the Rossmann algorithm^{49,50} as implemented in *LABELIT*⁵¹, with the choice of lattice basis guided by a target unit cell of $a = 118.2 \text{ \AA}$, $b = 224.6 \text{ \AA}$, $c = 331.9 \text{ \AA}$, $\alpha = \beta = \gamma = 90^\circ$ (later refined for data merging, Extended Data Table 1) for the dark and 2F-NH₃ PS II datasets. This cell was determined by examining the distribution of unit cell dimensions found when indexing with no target unit cell. Indexing was attempted on all frames, without a pre-filtering step, so as to obtain the maximal number of indexed images. As previously described in detail⁵² the Rossmann algorithm produces three basis vectors that generate a primitive triclinic lattice. Miller indices are then deduced for the strong spots, and the lattice parameters (unit cell and crystal orientation) are refined against the observed spot positions. Next, the lattice parameters are constrained to the known orthorhombic symmetry of the space group (in this case, $P_{2}1_2_1_2_1$), meaning the cell angles are all set to 90° , and the remaining free lattice parameters are re-refined. However, we noticed a potential problem with applying the orthorhombic constraints. In the earliest trials, we redetermined the Miller indices of the strong spots based on their proximity to lattice nodes, after applying the 90° constraints. We found that this can sometimes assign Miller indices that are misindexed by one unit along the c -axis, since the large $\sim 332 \text{ \AA}$ cell length gives lattice nodes that are very close together. We therefore incorporated a new option within *cctbx.xfel* to apply high-symmetry constraints, but skip the step of re-determining the Miller indices; instead, the initially determined Miller indices were converted from the triclinic to the high-symmetry setting using a change-of-basis operator⁵³ before performing the final round of parameter refinement. Refinement was implemented using the newly introduced *DIALS* toolkit⁵⁴, which implements

a target function based on both the observed spot positions and the reciprocal lattice points' angular proximity to the Ewald sphere⁵², while also permitting the refinement of additional parameters such as the detector tilt. As in previous work⁴⁸, strong spots not covered by the modelled lattice were considered separately in an attempt to index a second lattice on each image for the dark and 2F-NH₃ datasets. We note that different unit cell parameters were obtained for the higher resolution 2F data of native PS II collected at the XPP and the MXF instruments. Using the ADE–DOT method (Fuller, F. D. *et al.*, submitted) and slightly different dehydration conditions, an average unit cell of $a = 117.9 \text{ \AA}$, $b = 223.1 \text{ \AA}$, $c = 310.7 \text{ \AA}$, $\alpha = \beta = \gamma = 90^\circ$ was obtained, and a subsequent indexing step using these parameters as constraints was used to generate the final native PS II 2F dataset.

For the integration and merging of high-resolution reflections, we took into account various community concerns that weak reflections ought to be included since they contain measurable information⁵⁵, while at the same time realizing that shot-to-shot and crystal-to-crystal variation requires differing resolution cutoffs for each integrated image. For the work described here, the following solution was adopted: for each image, a first round of spot prediction and integration was performed, with a high-resolution cutoff based on the apparent limit of bright spots from the spotfinding program⁵⁶. The intensity/standard deviation ratio ($I/\sigma(I)$) was examined as a function of diffraction angle to determine the resolution bin where $\langle I/\sigma(I) \rangle = 0.5$, essentially identifying a zone within which the signal-to-noise falls to a low, but non-zero value. Then, for a second round of spot prediction and integration, the limiting resolution was set to a value far beyond the $\langle I/\sigma(I) \rangle = 0.5$ limit, in order to ensure that any reasonable positive signal was integrated. This ‘greedy’ integration limit was set to a reciprocal-spacing value that encloses 1.5 times as much reciprocal-space volume as the limit determined by $\langle I/\sigma(I) \rangle = 0.5$.

Based on the integrated intensity measurements from this second round of integration, individual resolution limits were then determined for each image as follows: $\langle I/\sigma(I) \rangle$ values were computed in resolution bins as a function of the diffraction angle, and the bins were excluded from further data merging beginning in the bin where $\langle I/\sigma(I) \rangle$ first falls below 0.1. This threshold, which is essentially zero, implies that measurements beyond the limiting bin are half positive and half negative on average, suggesting that no actual Bragg signal is present.

Before scaling and merging the dark and 2F-NH₃ datasets, images with a refined c axis that was not between 325 and 340 \AA were discarded. In the case of the native 2F dataset, the unit cell constraint during indexing ensured that no images with aberrant unit cells were integrated. Additionally, we examined the distribution of refined beam centres for all images. The beam centre (indicating the relation between the detector and the incident X-rays) is freely refined during parameter refinement, even though the true relative positions of the beam and detector are fixed to within a micrometre. The small fraction of images whose beam centre differed by more than one pixel from the mean were discarded, as these lattices were mis-indexed by one Miller index unit along a crystallographic axis, usually the long c axis. As the unit cell lengths of this crystal form differ from those of other PS II crystal forms reported elsewhere¹⁶, reference intensities for scaling were not available. We therefore merged and scaled the data initially without an external reference, using our postrefinement program *PRIME* recently described⁵⁷. A resolution cutoff of 2.5 \AA was chosen in this step to match the apparent resolution limit of the raw diffraction patterns. A total of 1,264, 22,311 and 2,294 diffraction images were included in the S₁-state, native 2F and the 2F-NH₃ datasets, respectively (Supplementary Table 1). Following merging and post-refinement, complete datasets for the dark, native 2F and 2F-NH₃ states were obtained at 3.0, 2.25 and 2.8 \AA resolution, respectively, and structural models were refined (see below for detailed description) to $R_{\text{work}}/R_{\text{free}}$ of 0.2637/0.3030 for the dark, 0.1949/0.2308 for the 2F and 0.2497/0.2997 for the 2F-NH₃ state (Extended Data Table 1, Supplementary Tables 2–4).

For the dark and 2F-NH₃ datasets an initial model was determined with *Phaser* molecular replacement⁵⁸ using two copies of a hybrid model of the PS II monomer composed of the cryogenic S₁-state PS II structure from *T. vulcanus* (PDB ID 4UB6⁷) and the additional chain present in native PS II from *T. elongatus* (PDB ID 4PJ0¹⁶). The initial model was refined using *phenix.refine*⁵⁹ and used to calculate model structure factors, which were then used as a scaling reference to re-scale the original data using the program *cxi.merge*. For the native 2F dataset the 2F-NH₃ model was used for *Phaser* molecular replacement. Examination of the $I/\sigma(I)$ and completeness measures as a function of resolution allowed us to select new resolution cutoffs at this stage and to re-merge the data with *cxi.merge* to these cutoffs. Negative measurements were included during merging instead of being discarded as had been done previously⁴⁸. Generally, including negative measurements moves the distribution of merged intensities closer to that expected for crystallographic data, as measured using the L and Z tests⁶⁰ (results not shown). Further investigation of this effect is ongoing and will be the subject of a future work.

Custom restraints for the Mn₄CaO₅ complex geometry for the dark state complex, derived from ref. 7, were generated by averaging bond lengths and angles over the four crystallographically independent monomers in two structures (PDB IDs 4UB6 and 4UB8) and imposing custom bond length and angle tolerances (see Supplementary Table 7 for restraints used). Average nonbonding distances between the cluster and surrounding residues were also calculated across the four monomers and adapted as restraints for the room temperature structures. Water molecules directly coordinating cluster metal atoms were restrained to match those in ref. 7 in early cycles of refinement, and these restraints were subsequently modified to minimize difference density, resulting in separate sets of metal–water restraints for the two crystallographically nonequivalent PS II monomers. Custom restraints were also generated for the α - and β -pucker chlorophyll-a ligands in order to effectively restrain the planarity of the porphyrin ring, the magnitude of displacement of the Mg centre from the plane of the ring, the direction of this displacement relative to the phytol tail (which differs between α - and β -pucker stereoisomers), and the Mg–His or Mg–water coordination distances at this medium resolution. The chlorophyll restraints were based on the default chlorophyll-a (CLA) ligand CIF file distributed with *Phenix*⁶¹. In the higher-resolution native 2F dataset, the data quality was sufficient to generalize to a single chlorophyll-a restraints file for both α - and β -puckers, but restraints maintaining coordination of chlorophyll magnesium atoms with nearby histidine sidechains or water molecules were still necessary to override the automatic repulsion of atoms within van der Waals distance of each other.

Model building and map calculation. Model building was performed in *Coot*⁶² and figures were generated using *PyMol* (Schrödinger, LLC). Model building was aided by recently-developed tools: feature-enhanced maps⁶³, designed to scale all non-solvent density to a uniform level, were used to identify highly flexible portions of ligands and detergent molecules once refinement had approached convergence⁵⁹. Polder omit maps (Liebschner *et al.*, submitted), a form of omit map newly available with the *Phenix* package, were used to test the contribution of model bias to the observed electron density at selected ligands and TMHs and to identify unmodelled water molecules in the vicinity of the Mn₄CaO₅ cluster. Polder omit maps are able to reveal weaker features than traditional omit maps by uniformly omitting bulk solvent from the omitted region and its surroundings, a key advantage when locating ordered solvent. To test model bias, polder omit maps were calculated after perturbing the model by omitting an area of interest: the selected ligand or residues were omitted, the resulting model was subjected to three cycles of coordinate and real space refinement in *phenix.refine*, the omitted ligand or residues were re-inserted (to allow identification of the region from which to omit bulk solvent), and the polder omit map was calculated (once again omitting the selected atoms in addition to the surrounding bulk solvent). Simulated annealing polder omit maps were calculated identically but with simulated annealing enabled during coordinate refinement. A comparison of normal $mF_o - DF_c$ and polder omit maps with real space or simulated annealing is shown in Extended Data Fig. 2e–h. The advantage of the polder compared to the $mF_o - DF_c$ map is manifested in lower noise and higher levels of detail of the electron density maps (compare Extended Data Fig. 2g, h). Comparing simulated annealing and real space polder omit maps for several different regions in the PS II complex (for example, Extended Data Fig. 2f, h) shows that both are very similar, with the simulated annealing being slightly more disruptive to the structure. As no additional benefit of the simulated annealing protocol was found, all other polder omit maps shown in this work were generated after real space refinement of the omit model.

Modelling of waters. Waters were incorporated into the model in two different steps. After initial refinement of the model, waters were placed into the $2mF_o - DF_c$ map using the *Phenix* auto water placement option during several subsequent coordinate refinement cycles. These positions were manually checked in *Coot*, and waters with strong enough electron density and good hydrogen bonding environments were then included in subsequent runs of refinement of the model with auto water placement disabled and coordinate and real space refinement enabled, resulting in 124, 1,179 and 107 ordered waters in the dark, 2F and 2F-NH₃ datasets, respectively (Extended Data Fig. 5). Upon convergence, polder omit maps excluding all waters were generated, and these were inspected for the placement of possible additional waters in the region around the OEC and within hydrogen bonding distance from hydrogen bonding-capable residues in the final model. For the two lower resolution datasets, waters were placed manually into polder maps in *Coot* and their positions were fit to the density using the *Coot* rigid body fit tool. The resulting model was subsequently refined for three cycles in *phenix.refine* with coordinate and real space refinement enabled. This resulted in an additional 33 and 55 water positions for the dark and 2F-NH₃ datasets, respectively (see for example, Extended Data Fig. 5d). The coordinates

for these additional waters are not included in the deposited PDB files but are given in Supplementary Table 6.

Estimated positional precision. To estimate the error when calculating differences in distances between cofactors, we sought to identify a method for determining the coordinate error of a molecule or residue sequence as a unit, for which the maximum likelihood estimate for atomic coordinate error (0.5 Å for our dark and 2F-NH₃ models, 0.34 Å for our native 2F model, 0.34 Å for 4PJ0 and 0.27 Å for 4UB6) is not a good guide. Instead we estimated the error in the positions of larger segments or molecules by generating simulated annealing omit maps of individual chlorophylls and TMHs. Treating the omitted unit as a rigid body, we obtained the best fit of the unit to polder difference density and calculated the magnitude of the shift as the distance between the centre of the unit in the refined model and the centre of the unit placed in the difference density. In the case of chlorophylls, the centre was defined as the average of the positions of the four porphyrin nitrogens, and in the case of the TMHs, the average of the positions of all α -carbons was used. On the basis of these results, we estimate that we can position an entire Chl molecule with better than 0.13 Å precision in the dark model and 0.10 Å in the 2F and 2F-NH₃ models. Similarly, for a TMH, we arrive at an upper bound of 0.08 Å precision for all three models. It is expected that the positional error should approach the maximum likelihood estimate for atomic coordinate error as the size of the unit decreases. Using the same procedure, the non-haem Fe^{II} shifted by 0.5–0.8 Å in the dark model, 0.0 Å in the 2F model and 0.3–0.5 Å in the 2F-NH₃ model.

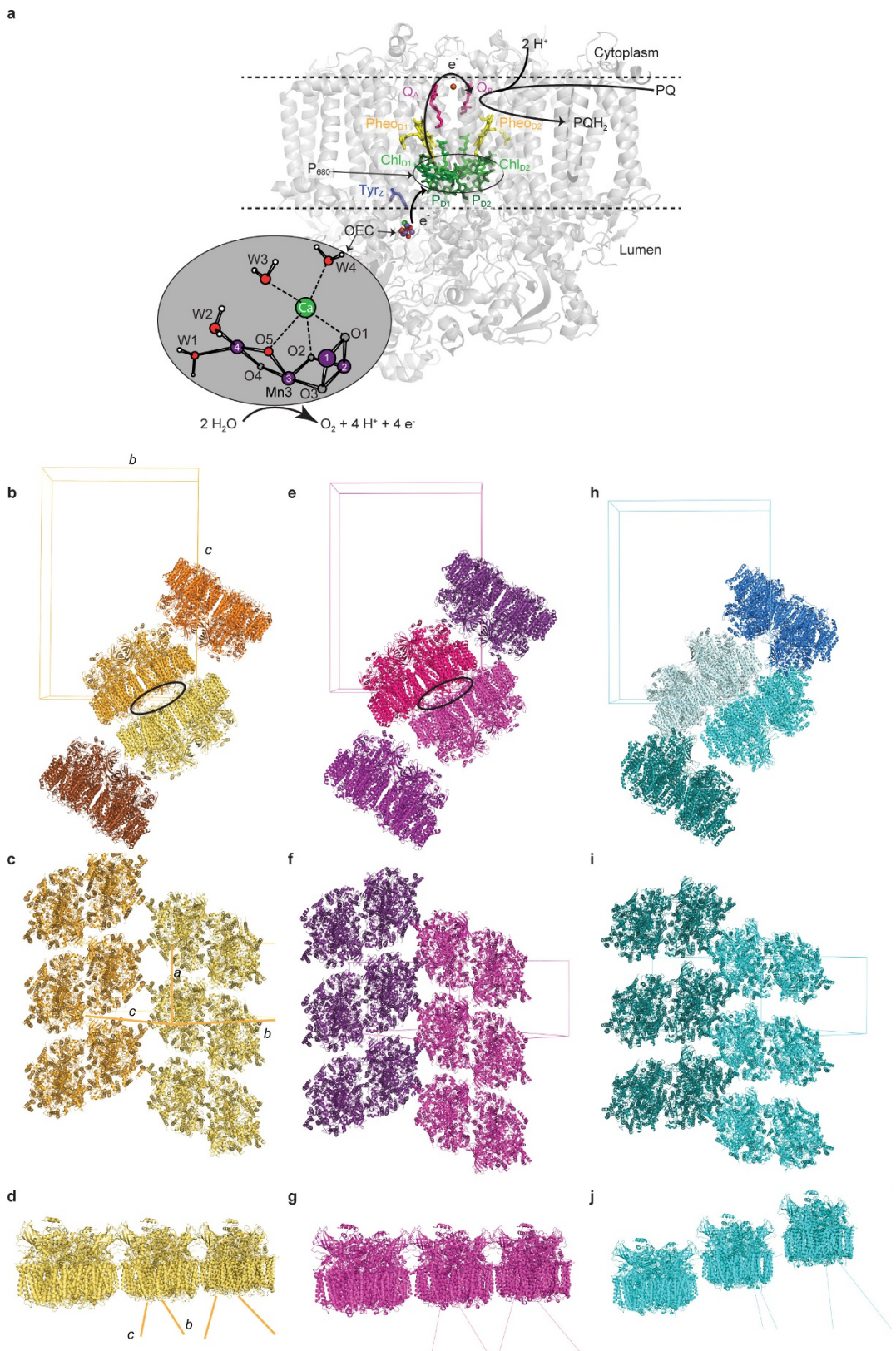
To estimate the precision of deriving the metal ion positions in the OEC, we compared a modification of the above technique and a difference-density generating technique. For the former, individual metal atoms were omitted from the cluster, but since polder maps are not applicable when omitting single atoms from a larger molecule, standard $mF_o - DF_c$ maps were used. Also, to prevent the collapse of coordinating waters into the cluster, waters coordinating Ca1 or Mn4 were omitted along with these atoms and restored to the annealed model before calculating $mF_o - DF_c$ maps. The mobile W4, which was placed after refinement and is not included in the deposited model for the dark and 2F-NH₃ datasets, was also added to the annealed model before map calculation for Ca1 only, since the difference density at the Ca1 centre was skewed in its absence. Observed shifts for each metal, averaged across the two monomers, ranged from 0.2 to 0.6 Å in the dark model, 0.1 to 0.6 Å in the 2F model and 0.2 to 0.4 Å in the 2F-NH₃ model. These values are likely to be overestimates owing to the propensity for the whole cluster to shift into the open density during refinement and for the surrounding, coordinated waters to affect the difference density.

For the difference-generating technique, we shifted individual metals in increments of 0.1 Å and calculated the resulting difference density ($mF_o - DF_c$). We propose that the magnitude of shift necessary to generate paired positive and negative difference density on either side of the atom can serve as an estimate of the positional error in OEC metal positions. A shift of Mn4 of 0.1 Å along the Mn4–Mn3 direction away from Mn3 led to paired difference density at the 2 σ contour level and a shift of 0.2 Å led to strong paired difference density at the 2.5 σ contour level in the lowest resolution dataset, clearly above the noise in the surrounding in the difference map. Combining the results from both approaches, we estimate the precision of our metal positions to be in the range of 0.2–0.4 Å for the dark model, 0.1–0.3 Å for the 2F model and 0.2–0.3 Å for the 2F-NH₃ model.

Comparison between the different PS II structures. Monomers or dimers of PS II from the 4UB6 and 4PJ0 models were superimposed onto our room temperature dark and 2F structural models using *Coot*. Cofactor distances were calculated as centre–centre distances. In the case of Chl and Pho, the centre was defined as the average of the positions of the four porphyrin nitrogens. To compare distances of cofactors from the pseudo C2-axis, the axis was defined as the membrane normal passing through the middle between the Pho_{D1} and Pho_{D2} molecules and distances of each pigment centre from this axis were computed. For comparison of individual residue positions, the models were aligned for short windows of 5–20 residues. For each of the two datasets, the quality of match between the $2mF_o - DF_c$ maps (together with the refined models) and the 4PJ0 or the 4UB6 models was inspected visually and scored. For several residues clear difference density was visible in the initial rounds of model building when the starting model (based on the cryogenic structures) was used for generation of the electron density maps. Additional, polder $mF_o - DF_c$ maps were used to inspect different rotamer conformations.

Code availability. Links to the software described here (*phenix*, *DIALS*, *cctbx.xfel*) and to specific instructions for processing XFEL data are given at <http://cci.lbl.gov>. **Data availability.** The atomic coordinates and structure factors have been deposited in the Protein Data Bank under accession numbers 5KAF (dark), 5TIS (2F) and 5KAI (2F-NH₃).

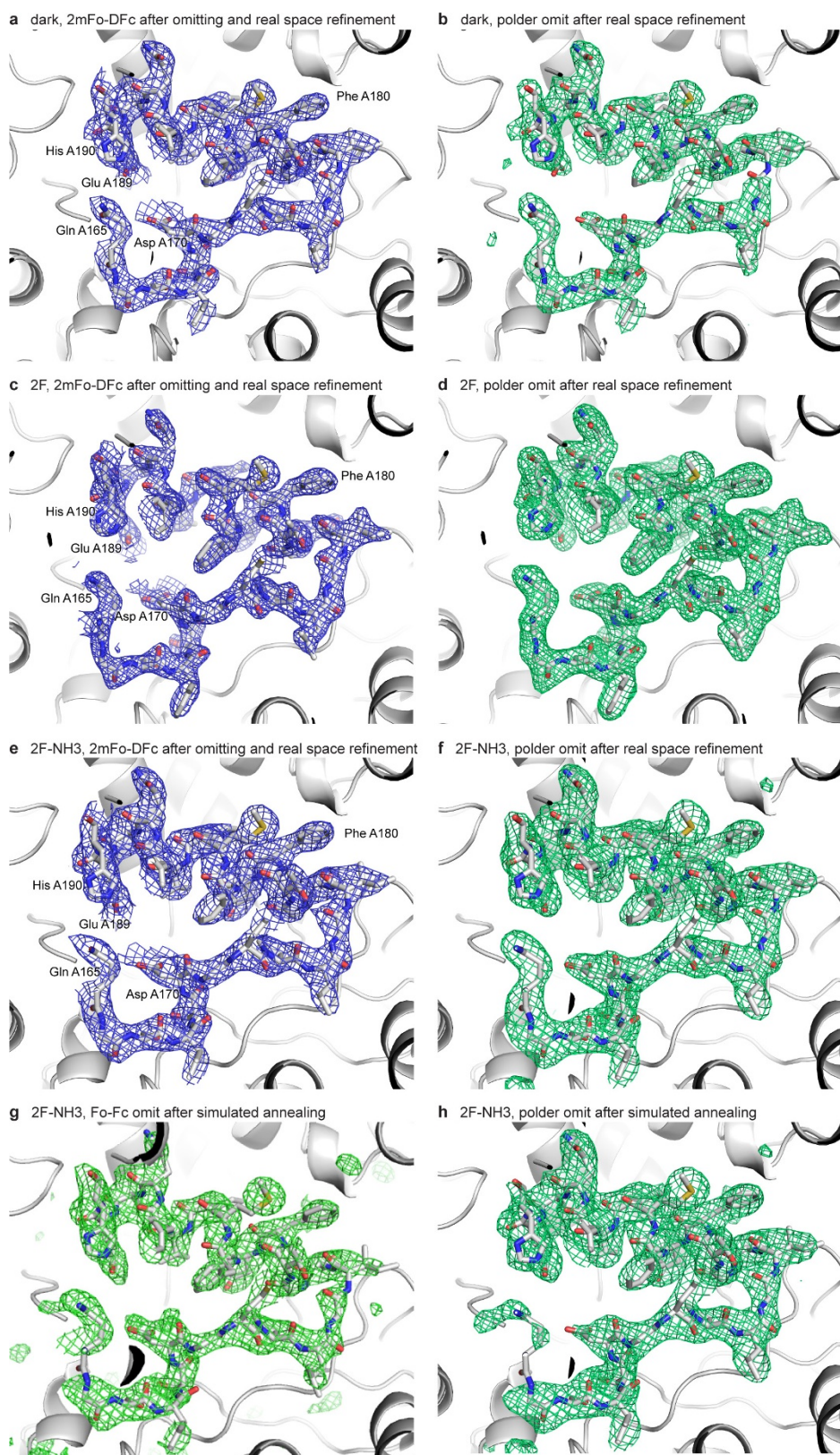
32. Kern, J. et al. Purification, characterisation and crystallisation of photosystem II from *Thermosynechococcus elongatus* cultivated in a new type of photobioreactor. *Biochim. Biophys. Acta* **1706**, 147–157 (2005).
33. Ibrahim, M. et al. Improvements in serial femtosecond crystallography of photosystem II by optimizing crystal uniformity using microseeding procedures. *Struct. Dyn.* **2**, 041705 (2015).
34. Pham, L. V. & Messinger, J. Electrochemically produced hydrogen peroxide affects Joliot-type oxygen-evolution measurements of photosystem II. *Biochim. Biophys. Acta* **1837**, 1411–1416 (2014).
35. Beck, W. F. & Brudvig, G. W. Binding of amines to the O₂-evolving center of photosystem II. *Biochemistry* **25**, 6479–6486 (1986).
36. Geijer, P., Deák, Z. & Styring, S. Proton equilibria in the manganese cluster of photosystem II control the intensities of the S(0) and S(2) state g ≈ 2 electron paramagnetic resonance signals. *Biochemistry* **39**, 6763–6772 (2000).
37. Yano, J. et al. in *Sustaining Life on Planet Earth: Metalloenzymes Mastering Dioxygen and Other Chewy Gases* Vol. 15 (eds Sosa Torres, M.E. & Kroneck, P.M.H.) 13–43 (Springer, 2015).
38. Beckmann, K., Messinger, J., Badger, M. R., Wydrzynski, T. & Hillier, W. On-line mass spectrometry: membrane inlet sampling. *Photosynth. Res.* **102**, 511–522 (2009).
39. Sierra, R. G. et al. Nanoflow electrospinning serial femtosecond crystallography. *Acta Crystallogr. D* **68**, 1584–1587 (2012).
40. Sierra, R. G. et al. Concentric-flow electrokinetic injector enables serial crystallography of ribosome and photosystem II. *Nat. Methods* **13**, 59–62 (2016).
41. Boutet, S. & Williams, G. J. The Coherent X-ray Imaging (CXI) instrument at the Linac Coherent Light Source (LCLS). *New J. Phys.* **12**, 035024 (2010).
42. Liang, M. et al. The Coherent X-ray Imaging instrument at the Linac Coherent Light Source. *J. Synchrotron Radiat.* **22**, 514–519 (2015).
43. Kern, J. et al. Simultaneous femtosecond X-ray spectroscopy and diffraction of photosystem II at room temperature. *Science* **340**, 491–495 (2013).
44. Chollet, M. et al. The X-ray Pump-Probe instrument at the Linac Coherent Light Source. *J. Synchrotron Radiat.* **22**, 503–507 (2015).
45. Boutet, S., Cohen, A. E. & Wakatsuki, S. The new macromolecular femtosecond crystallography (MFX) instrument at LCLS. *Synchrotron Radiat. News* **29**, 23–28 (2016).
46. Herrmann, S. et al. CSPAD upgrades and CSPAD V1.5 at LCLS. *J. Phys.* **493**, 012013 (2014).
47. Sauter, N. K., Hattne, J., Grosse-Kunstleve, R. W. & Echols, N. New Python-based methods for data processing. *Acta Crystallogr. D* **69**, 1274–1282 (2013).
48. Hattne, J. et al. Accurate macromolecular structures using minimal measurements from X-ray free-electron lasers. *Nat. Methods* **11**, 545–548 (2014).
49. Steller, I., Bolotovsky, R. & Rossmann, M. G. An algorithm for automatic indexing of oscillation images using Fourier analysis. *J. Appl. Crystallogr.* **30**, 1036–1040 (1997).
50. Rossmann, M. G. & van Beek, C. G. Data processing. *Acta Crystallogr. D* **55**, 1631–1640 (1999).
51. Sauter, N. K., Grosse-Kunstleve, R. W. & Adams, P. D. Robust indexing for automatic data collection. *J. Appl. Crystallogr.* **37**, 399–409 (2004).
52. Sauter, N. K. et al. Improved crystal orientation and physical properties from single-shot XFEL stills. *Acta Crystallogr. D* **70**, 3299–3309 (2014).
53. Sauter, N. K., Grosse-Kunstleve, R. W. & Adams, P. D. Improved statistics for determining the Patterson symmetry from unmerged diffraction intensities. *J. Appl. Crystallogr.* **39**, 158–168 (2006).
54. Waterman, D. G. et al. Diffraction-geometry refinement in the DIALS framework. *Acta Crystallogr. D* **72**, 558–575 (2016).
55. Sauter, N. K. XFEL diffraction: developing processing methods to optimize data quality. *J. Synchrotron Radiat.* **22**, 239–248 (2015).
56. Zhang, Z., Sauter, N. K., van den Bedem, H., Snell, G. & Deacon, A. M. Automated diffraction image analysis and spot searching for high-throughput crystal screening. *J. Appl. Crystallogr.* **39**, 112–119 (2006).
57. Uervirojnangkoorn, M. et al. Enabling X-ray free electron laser crystallography for challenging biological systems from a limited number of crystals. *eLife* **4**, e05421 (2015).
58. McCoy, A. J. et al. Phaser crystallographic software. *J. Appl. Crystallogr.* **40**, 658–674 (2007).
59. Afonine, P. V. et al. Towards automated crystallographic structure refinement with phenix.refine. *Acta Crystallogr. D* **68**, 352–367 (2012).
60. Padilla, J. E. & Yeates, T. O. A statistic for local intensity differences: robustness to anisotropy and pseudo-centering and utility for detecting twinning. *Acta Crystallogr. D* **59**, 1124–1130 (2003).
61. Adams, P. D. et al. PHENIX: a comprehensive Python-based system for macromolecular structure solution. *Acta Crystallogr. D* **66**, 213–221 (2010).
62. Emsley, P., Lohkamp, B., Scott, W. G. & Cowtan, K. Features and development of Coot. *Acta Crystallogr. D* **66**, 486–501 (2010).
63. Afonine, P. V. et al. FEM: feature-enhanced map. *Acta Crystallogr. D* **71**, 646–666 (2015).
64. Cox, N., Pantazis, D. A., Neese, F. & Lubitz, W. Biological water oxidation. *Acc. Chem. Res.* **46**, 1588–1596 (2013).
65. Isobe, H. et al. Theoretical illumination of water-inserted structures of the CaMn₄O₅ cluster in the S₂ and S₃ states of oxygen-evolving complex of photosystem II: full geometry optimizations by B3LYP hybrid density functional. *Dalton Trans.* **41**, 13727–13740 (2012).
66. Li, X., Siegbahn, P. E. M. & Ryde, U. Simulation of the isotropic EXAFS spectra for the S₂ and S₃ structures of the oxygen evolving complex in photosystem II. *Proc. Natl Acad. Sci. USA* **112**, 3979–3984 (2015).
67. Ichino, T. & Yoshioka, Y. Theoretical study on mechanism of dioxygen evolution in photosystem II. II. Molecular and electronic structures at the S₃ and S₄ states of oxygen-evolving complex. *Chem. Phys. Lett.* **595**, 237–241 (2014).
68. Hatakeyama, M. et al. Structural changes in the S₃ state of the oxygen evolving complex in photosystem II. *Chem. Phys. Lett.* **651**, 243–250 (2016).



Extended Data Figure 1 | See next page for caption.

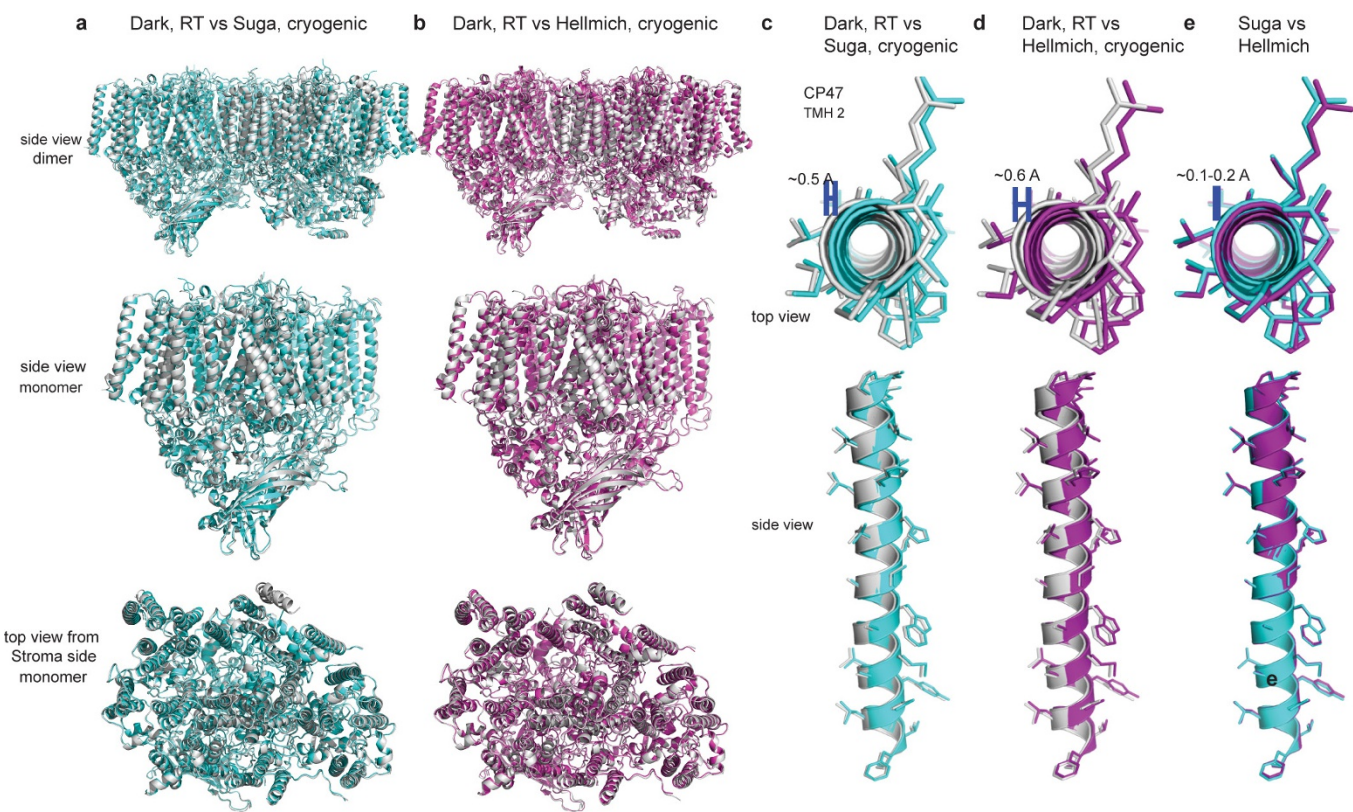
Extended Data Figure 1 | Schematic of the reaction centre and OEC in PS II and packing of the dimeric complex in the crystal lattice. **a**, The reaction centre is shown with cofactors labelled as Pheo (pheophytin), Chl (chlorophyll), PQ (plastoquinone), Q_A, Q_B (primary and secondary acceptor plastoquinones bound to PS II, respectively). The numbering of Mn (purple spheres), oxygen (red/grey spheres) atoms and metal-bound waters in the OEC follows the convention of ref. 21. Upon illumination of PS II, an electron is transferred $\sim 35\text{ \AA}$ across the membrane from the excited primary electron donor P₆₈₀ to the final electron acceptor Q_B via Chl_{D1}, Pheo_{D1}, Q_A, and a non-haem Fe^{II}. After accepting two electrons and undergoing protonation, plastoquinol Q_BH₂ is released from PS II into the membrane matrix. The photo-generated radical cation P₆₈₀^{•+} is reduced by a tyrosine residue (Tyr_Z) to generate a neutral tyrosine radical Tyr_Z[•], which acts as an oxidizing agent for water at the OEC. **b, c, d**, Packing of the dimeric complex observed in the room temperature data for three

different view directions. The unit cell is indicated by a wire frame and axes are labelled. Dimers related by translation are coloured identically. **e–g**, Packing observed in the cryogenic structure in ref. 16 (PDB: 4PJ0) in the same orientations as in **b–d**. **h–j**, Packing observed in the cryogenic XFEL structure in ref. 7 (PDB: 4UB6). The space group is the same in all three cases, but the unit cell dimensions and packing are different. Whereas the *a* and *b* dimensions are very similar between 4PJ0 and the current room temperature data, the *c* axis is elongated. This results in a very similar arrangement of dimers in rows along the *a* axis (compare **d** and **g**), whereas there is a larger spacing between two dimer rows at the cytoplasmic side of the complex (compare black ellipse in **b** and **e**) owing to the elongation of the *c* axis in the room temperature packing. The structure in ref. 7 has a very different arrangement of the dimers and no closely packed rows of dimers are visible (see **c** and **f** compared with **i**, and **d** and **g** compared with **j**).



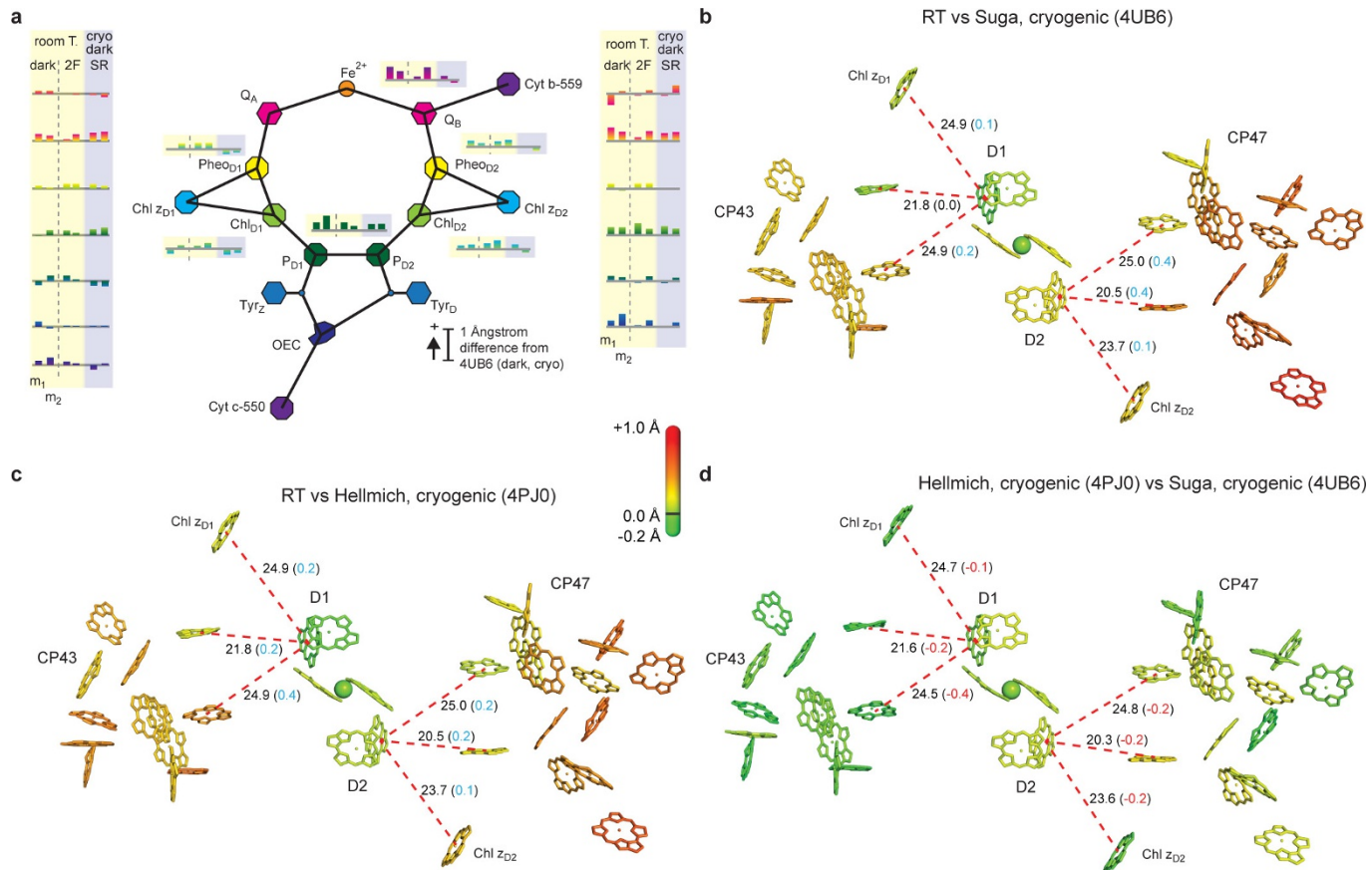
Extended Data Figure 2 | Electron density omit maps of the luminal CD helix and part of the loop region of subunit D1. **a–h**, Obtained from the room temperature dark (**a**, **b**), 2F (**c**, **d**), and 2F-NH₃ (**e**–**h**) datasets. For all maps residues 165–190 of subunit D1 (shown as grey sticks) were omitted followed by three rounds of coordinate and real space refinement of the model with (**g**, **h**) or without (**a**–**f**) simulated annealing in *phenix.refine*. **a**, 2mFo–DF_c map (blue, 1.5σ contour) of the dark dataset. **b**, Polder mFo–DF_c map (green, 4σ contour) of the dark dataset. **c**, 2mFo–DF_c

map (blue, 1.5σ contour) of the 2F dataset. **d**, Polder mFo–DF_c map (green, 4σ contour) of the 2F dataset. **e**, 2mFo–DF_c map (blue, 1.5σ contour) of the 2F-NH₃ dataset. **f**, Polder mFo–DF_c map (green, 4σ contour) of the 2F-NH₃ dataset. **g**, Standard mFo–DF_c omit map (green, 3σ contour) of the 2F-NH₃ dataset after simulated annealing. **h**, Polder mFo–DF_c map (green, 4σ contour) of the 2F-NH₃ dataset after simulated annealing.



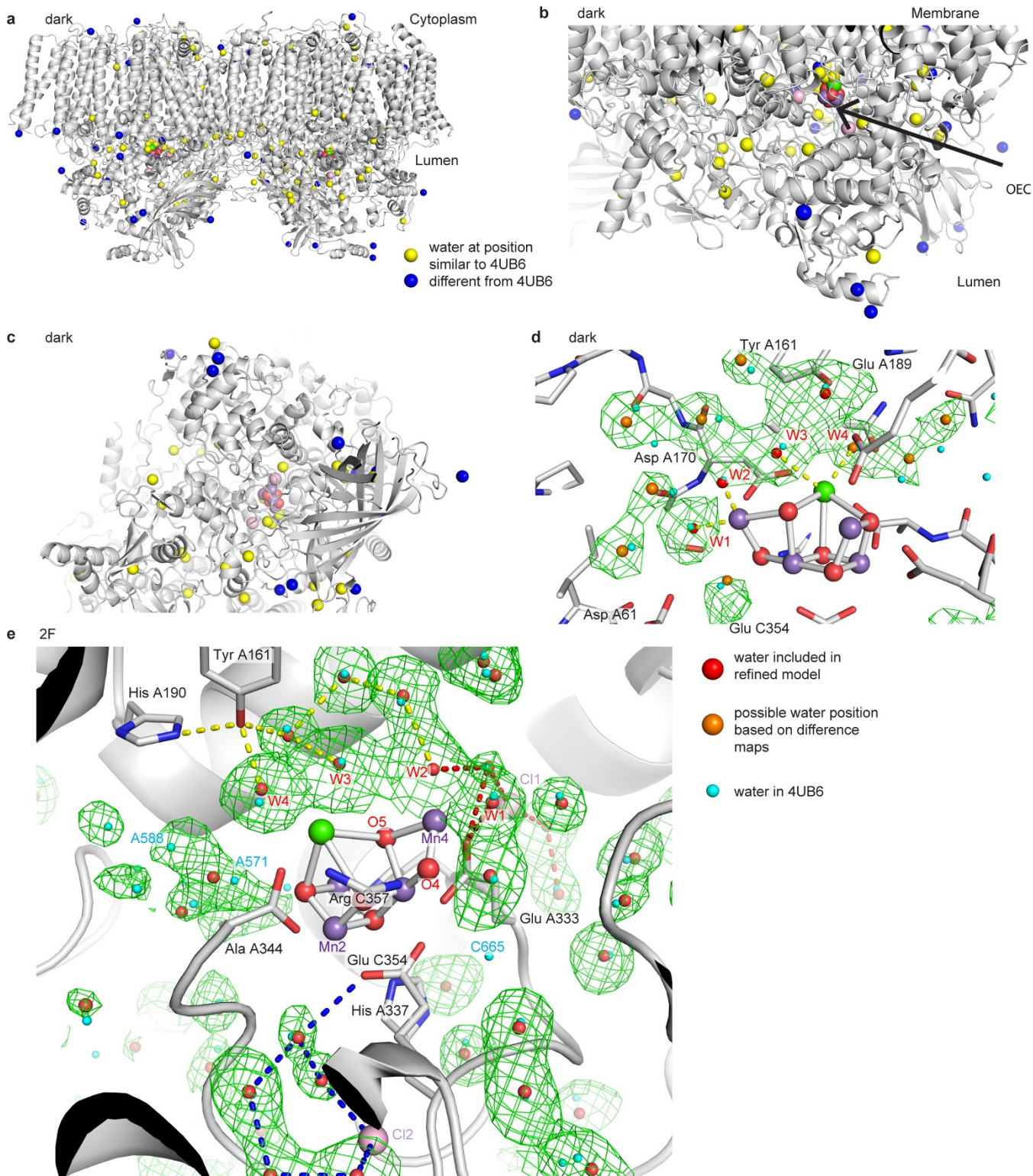
Extended Data Figure 3 | Comparison of dark room temperature structure with cryogenic structures from refs 7 and 16. Our room temperature dark state structure is shown in grey, the Suga XFEL⁷ in cyan and the Hellmich¹⁶ cryogenic structure in purple. **a**, Overlay of the room temperature and Suga⁷ structures. **b**, Overlay of the room temperature and Hellmich¹⁶ structures. A large-scale rigid body motion of the two monomers with respect to each other and an in-plane expansion of each PS II monomer in the room temperature structure are visible. **c–e**, Comparison of TMH 2 of subunit CP47 between the dark state and the cryogenic XFEL structure⁷ (**c**), the dark state and the Hellmich¹⁶

cryogenic structure (**d**) and between the two cryogenic structures (**e**). The two cryogenic datasets reflect crystals with different packing. View is from the cytoplasmic side (top) or along the membrane plane (bottom). Despite the different packing, only a small shift of 0.1–0.2 Å is observed between the two cryogenic structures. In contrast, the room temperature structure exhibits a larger shift of 0.5–0.6 Å in the positions of TMH 2 with respect to the cryogenic structures in both crystal forms, well above the error margin in our data. The cryogenic structures were superposed onto our dark structure model in PyMol (Schrödinger, LLC) using monomer 1 for alignment.



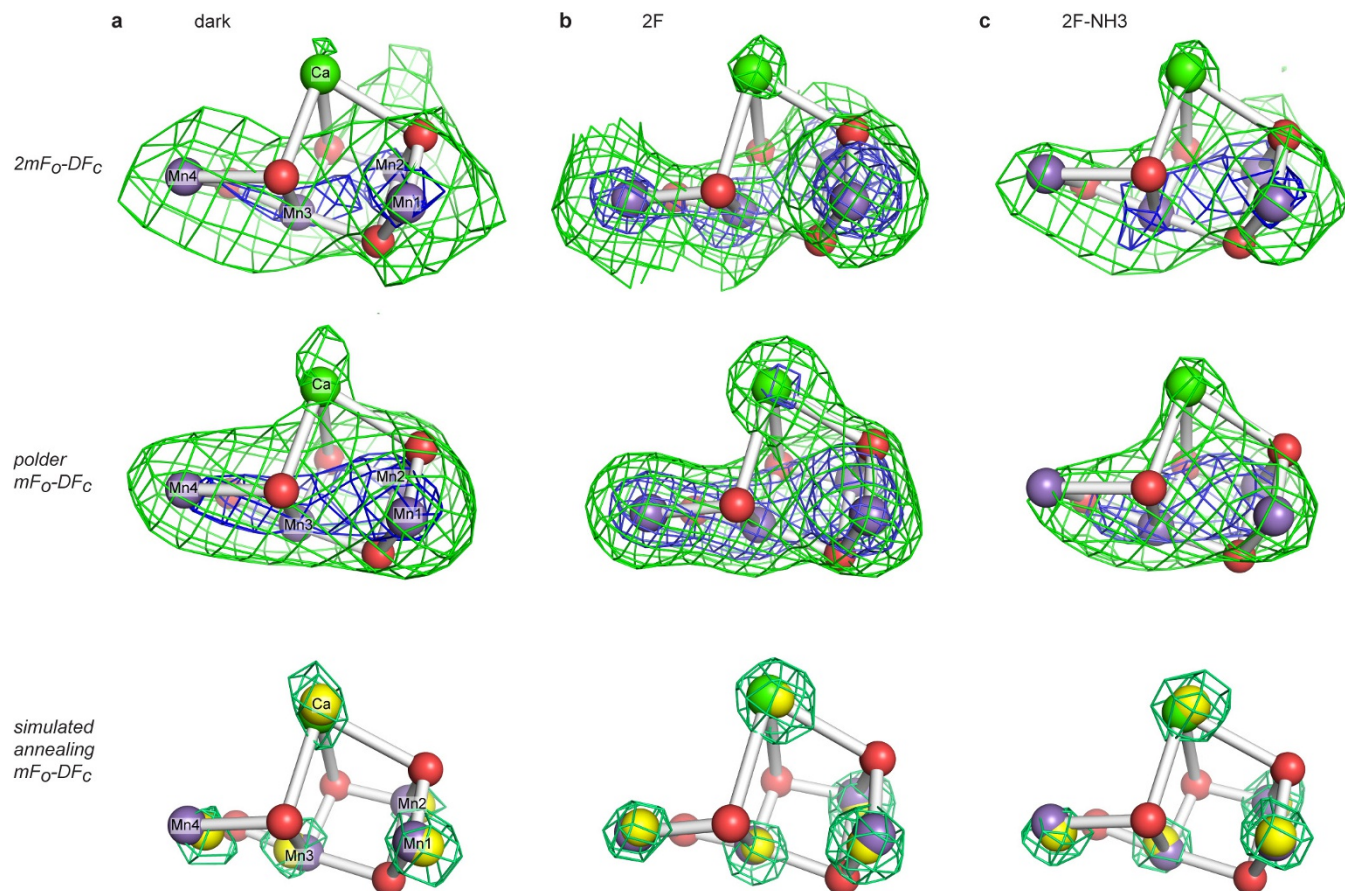
Extended Data Figure 4 | Comparisons of the cofactor–cofactor distances in the crystal structures collected at cryogenic temperature and room temperature. **a**, Distances for central cofactors; the histogram shows the deviation of the cofactor–cofactor distances in the Hellmich cryogenic SR dark state structure (4PJ0¹⁶, highlighted in blue) and in our dark and 2F room temperature structures (highlighted in yellow) from those of the cryogenic XFEL structure reported by Suga *et al.*⁷ (4UB6). Changes are indicated by bars for monomers 1 and 2 (m_1, m_2), and colour coding of bars matches the colouring of the associated pair of cofactors in the diagram. Among the differences, there is a consistent elongation in the distances involving Chl_z as well as in the Q_B–Cyt b-559 and OEC–Cyt c-550 distances of both monomers in the room temperature data. In other cases, expansion of individual cofactor distances is observed in both room

temperature structures and 4PJ0 relative to 4UB6 (for example, P_{D2}-Chl_{D2}, Q_B-Pheo_{D2}), and in the case of P_{D1}-P_{D2} on average the elongation is more pronounced at room temperature than in the cryogenic structures. Changes in Chl positions between the room temperature dark structure and 4UB6 (**b**), between the room temperature dark structure and 4PJ0, which have the same dimer-dimer packing (**c**), and between 4PJ0 and 4UB6 (**d**). The distances of the Chl ring centres from the membrane normal passing through the centre between Pheo_{D1} and Pheo_{D2} are computed and relative changes with respect to the values obtained from 4UB6 or 4PJ0 are shown as colour coding on a rainbow scale from green (0.2 Å contraction) to red (1.0 Å expansion). For selected Chl-Chl pairs, distances are given with the absolute change in parentheses.



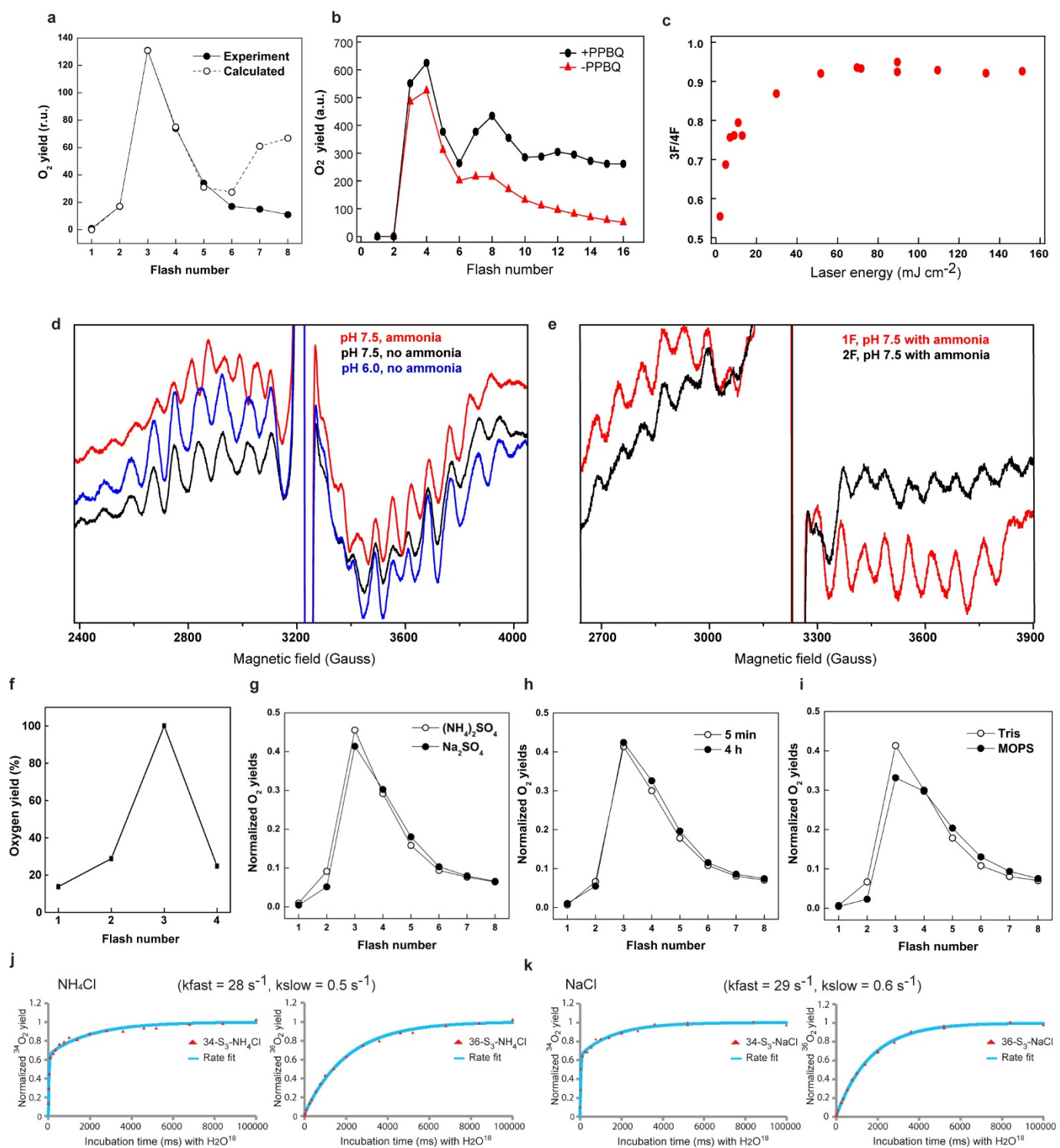
Extended Data Figure 5 | Location of water molecules observed in the room temperature structure. **a**, Water positions refined in the dark room temperature structure of the PS II dimer are indicated by blue and yellow spheres. View is along the membrane plane with the cytoplasm on top and lumen on the bottom. Waters whose positions coincide with waters located in the cryogenic XFEL structure⁷ (4UB6) are coloured in yellow and waters in other positions are coloured in dark blue. **b**, Enlarged view of the luminal region showing the OEC of one monomer (magenta, red and green spheres for Mn, O and Ca) as well as the two Cl^- (pink spheres) located close to the OEC. **c**, Waters located at the luminal side of one monomer. View is from the luminal side onto the membrane plane, with colour coding as in **a** and **b**. **d**, Polder omit maps (2.5σ contour, green

mesh) for waters in the direct vicinity of the OEC in the dark state. Waters included in the refined model are indicated as red spheres, additional waters placed based on polder maps as orange spheres, and waters from 4UB6 are shown in light cyan. **e**, Possible water networks next to the OEC. Waters included in the refined model of the 2F state are indicated as red spheres and waters from 4UB6 are shown in light cyan. Polder omit maps (2.0σ contour, green mesh, carved at 2 \AA around water positions from 4UB6) confirm the positions of the refined waters and indicate the presence of additional waters (for example, A571, A588), but no omit map density was observed at the position of water C665. The starting points of three water/proton channels postulated in ref. 21 are indicated by dashed red, yellow, and blue lines.



Extended Data Figure 6 | Room temperature electron density of the Mn_4CaO_5 cluster. **a**, The $2mF_o-DF_c$ electron density (top) contoured at 4.0σ (green) and 8.0σ (blue mesh) and the polder mF_o-DF_c electron density (middle) of the dark dataset after omitting the OEC and real space refinement contoured at 8.0σ (green) and 14.0σ (blue mesh). At the bottom, the mF_o-DF_c electron density after omitting individual metal atoms and refining with simulated annealing is shown contoured at 4.0σ (Ca), 7.0σ (Mn1, Mn2), 8.0σ (Mn3) and 4.0σ (Mn4). The model of the OEC is shown with Mn as magenta, Ca as green and oxygen as red spheres overlaid with yellow spheres indicating the centres of the obtained omit densities. **b**, The $2mF_o-DF_c$ electron density (top) contoured at 3.0σ (green) and 6.0σ (blue mesh) and the polder mF_o-DF_c electron

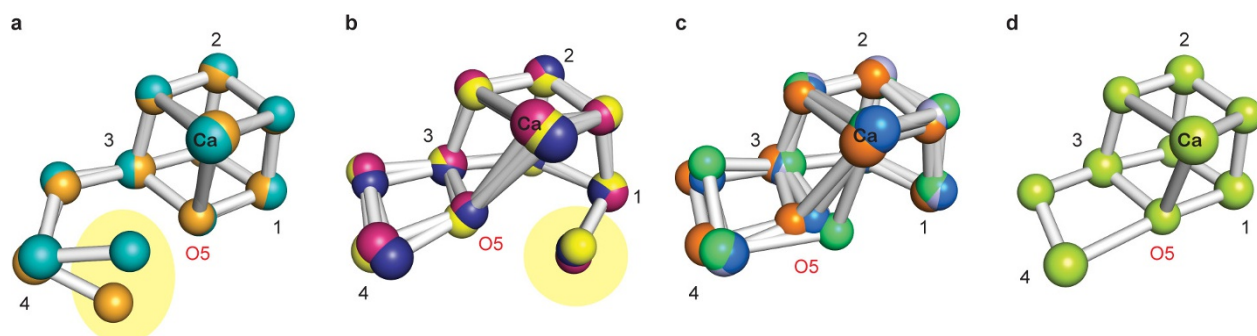
density (middle) of the 2F dataset after omitting the OEC and real space refinement contoured at 8σ (green) and 14σ (blue mesh). At the bottom, the mF_o-DF_c electron density after omitting individual metal atoms and refining with simulated annealing is shown contoured at 12.0σ (Ca, Mn1, Mn3), 13.0σ (Mn2) and 10.0σ (Mn4), with colour coding as in **a**. **c**, The $2mF_o-DF_c$ electron density (top) contoured at 5.0σ (green) and 8.0σ (blue mesh) and the polder mF_o-DF_c electron density (middle) of the 2F-NH₃ dataset after omitting the OEC and real space refinement contoured at 11σ (green) and 16σ (blue mesh). At the bottom, the mF_o-DF_c electron density after omitting individual metal atoms and refining with simulated annealing is shown contoured at 5.0σ (Ca), 10.0σ (Mn1), 8.0σ (Mn2, Mn4) and 11.0σ (Mn3), with colour coding as in **a**.



Extended Data Figure 7 | See next page for caption.

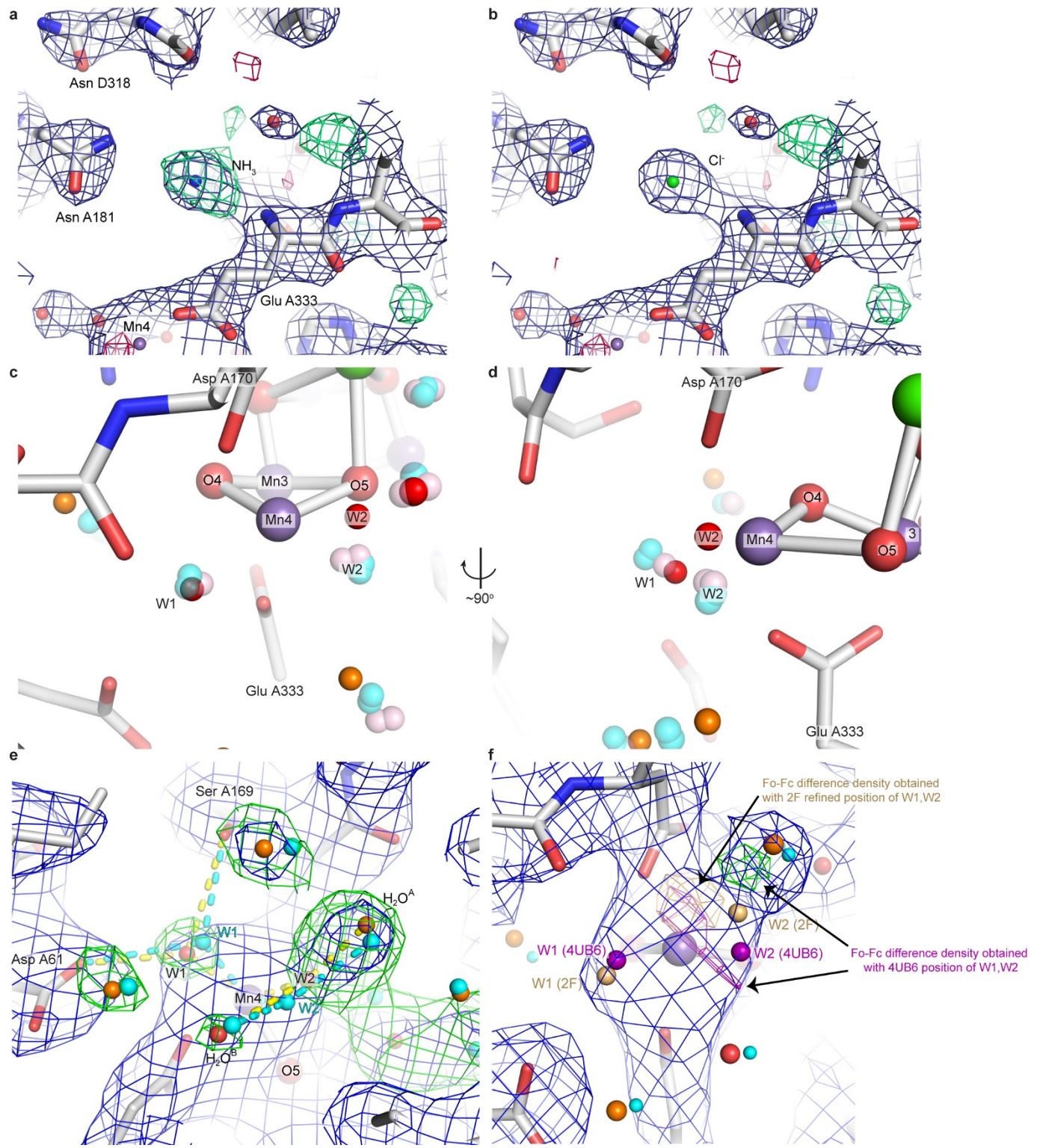
Extended Data Figure 7 | Characterization of PS II samples and substrate water exchange rates in the S₃ state. **a**, Flash-induced O₂ evolution pattern (FIOP) of a suspension of the native PS II core complexes (PSIIcc) at pH 6.5. Fit parameter: 100% S₁ in the dark, miss 20%, double hit 4%, damping 2%, fit done on first five flashes. In the 2F sample, if double hits are excluded, ~60% of the S₃ population was calculated, with ~30% of S₂ and ~4% of S₁. **b**, FIOP of a suspension of the PS IIcc (TRIS, pH 7.5, 100 mM (NH₄)₂SO₄) with and without PPBQ measured with 12 s between flashes using the thin layer MIMS setup (see Methods) and 532 nm laser flash illumination: an increase in O₂ yield by 15% was observed if PPBQ was added. **c**, Light saturation in the thin layer MIMS set up resembling the illumination conditions of the DOT approach. The ratio of the oxygen yield of the third flash over that of the fourth flash is plotted as a qualitative measure for the miss parameter, which is minimal when the ratio is large. **d**, EPR spectra of native (pH 6.0 and 7.5) and ammonia-treated (pH 7.5) PS II solutions after continuous illumination at 195 K for 1 min followed by annealing to 260 K for 30 s. Spectrometer condition: microwave frequency, 9.23 GHz; field modulation amplitude, 32 G at 100 KHz; microwave power, 20 mW. The spectra were collected at 7 K. **e**, EPR spectra of ammonia-treated (pH 7.5) PS II solution after applying one (red) or two (black) flashes. Spectrometer conditions are as in **a**. **f**, O₂-flash pattern of PS II crystals at pH 7.5 (TRIS, (NH₄)₂SO₄) measured by MIMS with the replica set up for jet illumination described above. **g**, FIOP (Joliot-type electrode) of PSIIcc at pH 7.5 and 20 °C in TRIS buffer with either 100 mM (NH₄)₂SO₄ or 100 mM Na₂SO₄ addition.

The O₂ yields for each sample were normalized to the O₂ yields induced by flashes 3–6 (Y3–6). No artificial electron acceptors were added. The flash frequency of the Xe-flash lamp was 2 Hz, and the Chl concentration 0.4 mM. Data are the average of three technical replicates. From the data, a miss parameter of 23–25% and an S₃ state population of 50–53% can be extracted for both sample types. Double hits, caused by the Xe flash lamp, are 3–6%, and are absent under laser flash illumination used during the XFEL experiments. The total O₂ yield of the ammonia-containing sample was 66% of the Na₂SO₄ control, and 52% of the FIOP at pH 6.5 (**a**). **h**, FIOP of PS II core sample incubated in TRIS and 100 mM (NH₄)₂SO₄ for 5 min at pH 7.6 versus one that was incubated for 4 h at room temperature. No degradation of the sample was observed over time (O₂ yields of both FIOPs normalized to Y3–6 of 4-min trace). **i**, FIOP of PS II core sample containing TRIS and 100 mM (NH₄)₂SO₄ versus one containing MOPS and 100 mM (NH₄)₂SO₄. Both FIOPs normalized to Y3–6 of TRIS containing sample. **j**, **k**, Substrate water exchange was measured for the S₃ state of PS II core complexes at pH 7.6/20 °C as described^{2,4,12} in HEPES buffer containing 100 mM NH₄Cl (**j**) or 100 mM NaCl (**k**). The left panels show the biphasic rise of the mass 34 peak (¹⁶O¹⁸O), while the right side shows the simultaneously recorded monophasic rise of the 36 peak of the double exchanged ¹⁸O¹⁸O. Red symbols represent the individually measured data points, while the blue lines are the kinetic simulations. Nearly identical rates for the exchange of the fast (k_{fast}) and slow (k_{slow}) substrates were found with and without ammonia.



Extended Data Figure 8 | Possible Mn_4CaO_5 complex models for the S_3 -state proposed in the literature. The models are grouped into four classes (a–d, see below). Mn are numbered (1–4) as in the main text. **a**, Models with an inserted water (highlighted in yellow) on the left side (closed cubane proposed as a transient S_3 -state in ref. 64 in teal; ref. 65 in light orange) shift Mn4 the furthest out. **b**, Models with an inserted water (highlighted in yellow) on the right side (model in ref. 64 in yellow; ref. 66 in pink; ref. 67 in dark blue) closely resemble models with an open cubane, and were proposed initially by Li and Siegbahn²³. **c**, Other models

with no inserted water: from ref. 67 in marine blue; 4UB6⁷ in green; from ref. 67 in lavender; from ref. 65 in dark orange). **d**, Only one proposed model featured a closed cubane with no inserted water (ref. 68 in yellow-green). Note that, except for the type **a** structure (a complete cubane plus mono- μ -oxo bridged Mn4) and the type **d** structure (a closed cubane with no water inserted), the Mn atomic positions are very similar in all models within 0.26 Å. Even between the type **a** and other models, the Mn4 positions differ only by 0.73 Å. On the other hand, the O5 position is expected to differ among the models by at most 1.52 Å.



Extended Data Figure 9 | See next page for caption.

Extended Data Figure 9 | The electron density of the Cl⁻ binding sites and environment of the W1 and W2 sites at the OEC in the 2F-NH₃ samples in the 2F dataset. **a**, The Cl⁻ binding site 1 with Cl⁻ (green sphere) at its refined position. The $2mF_o - DF_c$ map (blue mesh) is shown at 1.5σ , and the $mF_o - DF_c$ map (green/red) is shown at $\pm 3\sigma$. **b**, Cl⁻ binding site 1 with ammonia (blue sphere) instead of Cl⁻ included in the model. The lack of difference density at the Cl⁻ position in the refined model and the positive difference density observed when ammonia is substituted for Cl⁻ indicate that ammonia does not account for the electron density and that Cl⁻ is a good model for the observed density. **c, d**, Comparison of the positions of W1 and W2 among the 2F-NH₃ (red), 2F (light pink) and cryogenic S₁-XFEL⁷ (light cyan) structures in two different orientations. The outcome of two different alignment procedures (to optimize overlap of either OEC Mn atoms or the surrounding protein ligands) are shown, illustrating the error in these alignments. A small shift of both W1 and W2 upon transition from the cryogenic S₁-XFEL to the 2F structure is visible. In the 2F-NH₃ model, W1 is shifted slightly

further along the same direction as the dark-2F difference. In contrast, the displacement of W2 in the 2F-NH₃ model is significantly larger than that between the S₁-XFEL and 2F structures. **e**, $2mF_o - DF_c$ electron density (blue, 1.0σ) of the 2F-NH₃ dataset around Mn4, and polder omit maps at 3.5σ (green). Red spheres, water refined in the current model; orange spheres, water placed in the polder maps but not included in the refined model; cyan spheres, water positions from the cryogenic XFEL structure. **f**, When calculating the $mF_o - DF_c$ electron density using the refined positions of W1 and W2 (light orange spheres) from the 2F-NH₃ data, only a negative peak is observed (orange mesh, -3σ contour) while using W1 and W2 positions (purple spheres) from the S₁-XFEL structure yields clear positive and negative peaks (green and purple mesh, $\pm 3\sigma$ contour, colouring of other waters as in **e**). This indicates that the W2 position from the S₁-XFEL structure does not provide a good fit to the observed electron density. However, at the present resolution the observed difference densities may be influenced by other effects, for example, Fourier series truncations and the strong density of H₂O^A close to W2.

Extended Data Table 1 | Data collection and refinement statistics for the room temperature dark (S_1), 2F and 2F-NH₃ data

	S_1 dataset (5KAF)	2F dataset (5TIS)	2F-NH ₃ dataset (5KAI)
Data collection			
Space group	$P2_12_12_1$	$P2_12_12_1$	$P2_12_12_1$
Cell dimensions			
<i>a, b, c</i> (Å)	117.7±1.2, 223.8±2.5, 330.8±2.6	117.9, 223.1, 310.7 ^a	117.9±1.6, 224.3±3.3, 331.0±2.9
α, β, γ (°)	90, 90, 90	90, 90, 90	90, 90, 90
Wavelength (Å)	1.7493	1.3010	1.7492
Resolution (Å)	43.13-3.00 (3.05-3.00) ^b	44.28-2.25 (2.29-2.25)	43.58-2.80 (2.85-2.80)
Unique reflections	170444 (7698)	385065 (19084)	213400 (10235)
Completeness (%)	97.30 (88.80)	99.98 (99.98)	99.00 (95.96)
Multiplicity	8.48 (2.91)	158.47 (10.36)	13.70 (4.17)
<i>I</i> / $\sigma(I)$	10.51 (2.26)	19.83 (2.04)	11.62 (1.94)
<i>CC</i> _{1/2}	53.2 (13.2)	97.4 (1.8)	54.2 (7.3)
Wilson B-factor	61.05	42.98	60.41
Collection instrument	LCLS endstation CXI	LCLS endstations XPP and MFX	LCLS endstation CXI
Refinement			
<i>R</i> _{work} (%)	26.37 (33.50)	19.49 (34.04)	24.97 (33.98)
<i>R</i> _{free} (%)	30.30 (37.98)	23.08 (38.09)	29.97 (33.98)
No. atoms	50162	51757	50284
Protein residues	5319	5319	5316
Ligands	174	189	180
Waters	124	1179	107
Average <i>B</i> factor	47.3	45.9	56.6
R.m.s. deviations			
Bond lengths (Å)	0.004	0.005	0.004
Bond angles (°)	0.479	0.502	0.592
Ramachandran favored (%)	96.18	97.20	95.20
Ramachandran outliers (%)	0.19	0.29	0.57
MolProbity clashscore	4.45	4.45	6.55

^aUnit cell parameters were constrained for this dataset.^bValues in parentheses are for the highest-resolution shell.